Supercritical ethanol–CO_2 mixtures exhibit microscopic immiscibility: A combined study using X-ray scattering and molecular dynamics simulations

Jingcun Fan,*,† Taekeun Yoon,† Guillaume Vignat,† Haoyuan Li,† Khaled Younes,†
Arijit Majumdar,† Priyanka Muhunthan,† Dimosthenis Sokaras,‡ Thomas Weiss,‡
Ivan Rajkovic,‡ and Matthias Ihme*,†,‡,¶

†*Department of Mechanical Engineering, Stanford University, Stanford, CA, 94305, USA*
‡*SLAC National Accelerator Laboratory, Menlo Park, CA, 94025, USA*
¶*Department of Energy Science and Engineering, Stanford University, Stanford, CA, 94305, USA*

E-mail: jcfan@stanford.edu; mihme@stanford.edu

Abstract

Supercritical mixtures of ethanol (EtOH) and carbon dioxide (CO_2) are classified as type-I mixtures, with complete macroscopic miscibility. However, differences in molecular polarity and interactions suggest a distinct phase behavior at the microscopic level. Here, we combine Small Angle X-ray Scattering experiments and molecular dynamics (MD) simulations to investigate the microscopic structure of EtOH–CO_2 mixtures under supercritical conditions. The structure factor exhibits non-linear composition-dependent behavior, revealing pronounced local density fluctuations. The complementary MD simulations, using optimized force field parameters, provide atomistic insight, showing that EtOH forms self-associated, hydrogen-bonded aggregates, while CO_2 remains more uniformly distributed. Cluster analysis identifies a preferential EtOH-rich composition exceeding the bulk average, governed by a balance between energetic and entropic competition. These results demonstrate that, contrary to macroscopic expectations, the mixture exhibits significant microscopic heterogeneity and immiscibility, which may influence solubility, reactivity, transport properties, and thermodynamic response functions. These findings challenge the conventional views of type-I fluids and emphasize the necessity of revising mixture states and considering molecular polarity.

Graphical TOC Entry

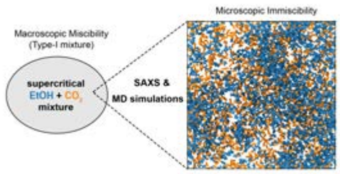

Understanding the microscopic structure of supercritical fluids is crucial for manipulating their macroscopic properties, optimizing industrial processes, and developing new applications across scientific and technological fields.[1–4] While these applications typically involve mixtures of different fluids, most studies on the microscopic structure of supercritical fluids have focused on pure fluids.[5,6] A supercritical mixture of particular interest is the system involving ethanol (EtOH) and carbon dioxide (CO_2), which has a broad spectrum of applications, including supercritical extraction,[7,8] supercritical drying of aerogels,[9] de-oiling,[10] and pharmaceutical processes involving enhanced drug solubility.[11] Knowledge of the microscopic structure and phase behavior in EtOH-CO_2 mixtures is therefore essential for elucidating and optimizing the solubility, transport properties, and reactivity of solutes in these applications.

Supercritical binary mixtures are conventionally classified by projections of their critical curves onto the x-P-T state space,[12–14] where x is the mole fraction of one component, P is pressure, and T is temperature. This classification groups mixtures into distinct types from a macroscopic viewpoint, based on their equations of state and corresponding mixing rules.[15–17] Type-I mixtures are characterized by a continuous liquid-gas critical line that connects the critical points of each pure component (e.g., EtOH-CO_2), indicating complete liquid-liquid miscibility across all temperatures. Type-II mixtures also exhibit a continuous critical line but additionally display regions of liquid–liquid immiscibility at temperatures below the critical line (e.g., CO_2-octane). Type-III mixtures feature disconnected critical lines and exhibit liquid–liquid immiscibility in the gap between them (e.g., neon–krypton).

The supercritical EtOH-CO_2 mixture is a typical type-I mixture, characterized by complete miscibility.[18,19] Similar to pure fluids, such mixtures are also characterized by a single Widom line that delineates the transition from a high-density, liquid-like state to a low-density, gas-like state.[14] Under this framework, one may expect EtOH and CO_2 molecules to possess microscopic distributions with high similarity at equilibrium. However, while EtOH is a polar solvent with a strong tendency to form hydrogen bonds,[20] CO_2 is a non-polar molecule with weak van der Waals interactions.[21,22] This contrast in polarity suggests that, despite macroscopic miscibility, the two components may exhibit different mixing behaviors at the microscopic level. Indeed, studies have shown that the thermodynamic factor reaches a minimum near the Widom line of type-I mixtures,[23–26] consistent with large density fluctuations and pronounced clustering,[27] pointing to strong thermodynamic non-idealities. Experimental and theoretical studies on the local intermolecular structure of EtOH-CO_2 mixtures have revealed two key structural features: strong hydrogen-bonded EtOH aggregation and the formation of weak electron donor-acceptor complexes between EtOH and CO_2.[28–32] Molecular dynamics (MD) simulations have shown that the minimum of the thermodynamic factor and large variations in transport properties of EtOH-CO_2 mixtures near the Widom line are strongly influenced by EtOH self-association.[25]

The hydrogen bond statistics in EtOH-CO_2 mixtures has been investigated through a combination of nuclear magnetic resonance (NMR) spectroscopy and molecular simulations,[33] indicating that hydrogen bonding in the mixture is highly dependent on temperature and composition. Mixed cluster formation is also observed in the Widom delta region from non-linear refractive index measurements and MD simulations.[34,35] While these findings suggest the presence of microscale heterogeneities in supercritical EtOH–CO_2 mixtures—challenging the conventional notion of uniform miscibility in type-I systems at all scales—most of the existing studies rely heavily on theoretical calculations and MD simulations. Direct experimental studies that probe the microscopic structure of these mixtures remain scarce. Moreover, most efforts have focused on CO_2-rich compositions in the liquid-like supercritical region, leaving significant gaps in our understanding of microscopic phase behavior across a broader thermodynamic range. Consequently, a systematic exploration ranging from liquid-like to gas-like supercritical states, combined with explicit structural characterization, is necessary to elucidate the influence of composition, temperature, and intermolecular interactions on the microstructural organization of these mixtures.

Motivated by these observations, we investigate the microscopic structure of supercritical EtOH-CO_2 mixtures using a combination of Small Angle X-ray Scattering (SAXS) experiments and MD simulations. Structure factors for mixtures with EtOH mole fractions of x $= 0$, 0.5, 0.7, and 1.0 are measured with SAXS over a range of temperatures at 147 bar. These measurements reveal a non-linear behavior in the structure factor, indicating that the microscopic interactions in the mixture give rise to unique density heterogeneities and clustering phenomena that cannot be described by a simple linear superposition of the pure components' behavior. The heterogeneous mixing behavior is further elucidated from MD simulations by computing partial structure factors and analyzing the clustering behavior of the mixture.

The SAXS measurements were conducted at the Stanford Synchrotron Radiation Lightsource (SSRL) Beamline 4-2[36] with a photon energy of 15 keV and a corresponding wavelength of $\lambda = 0.827$ Å. The experimental setup is shown in Figure 1. The scattered X-ray photons were collected with an area detector (Dectris Pilatus3 X 1M) with a Q-range of 0.05 to 2.0 Å^{-1}, where $Q \equiv {}^{4\pi}/_{\lambda} \sin({}^{\theta}/_{2})$ is the momentum transfer. Here, θ indicates the X-ray scattering angle as shown in Figure 1(a). The EtOH-CO_2 mixture was contained in a pressure cell[37] made of titanium alloy, selected for its chemical stability at elevated pressure and temperature. The X-ray entrance and exit windows were sealed with diamond windows (Applied Diamond, Wilmington, DE, USA) of 100 µm thickness. The mixture temperature was measured with a K-type thermocouple (Omega Engineering, Norwalk, CT, USA) inside the pressure cell and maintained by eight cartridge heaters (Briskheat, Columbus, OH, USA) at a precision of ± 0.1 K and an accuracy of ± 2.5% at the least accurate high-temperature condition. The mixture pressure was measured and maintained with external syringe pumps (Teledyne ISCO 100DM, Lincoln, NE, USA). Figure 1(b) summarizes the measured x-P-T conditions in the phase space of EtOH-CO_2 mixture. Measurements were conducted at a fixed pressure of 147 bar, for pure EtOH and CO_2 and their mixtures at $x = 0.5$ and 0.7. This pressure is chosen to ensure the system remains in the supercritical regime throughout the entire temperature range. At each temperature, the system was stabilized for 10 minutes to achieve thermal equilibrium before performing SAXS measurements. Scattering intensities with an empty sample cell were measured at all temperatures for background subtractions. See supporting information (SI) for the details on the sample preparation procedure and the conversion from scattering intensity, $I(Q)$, to structure factor, $S(Q)$.

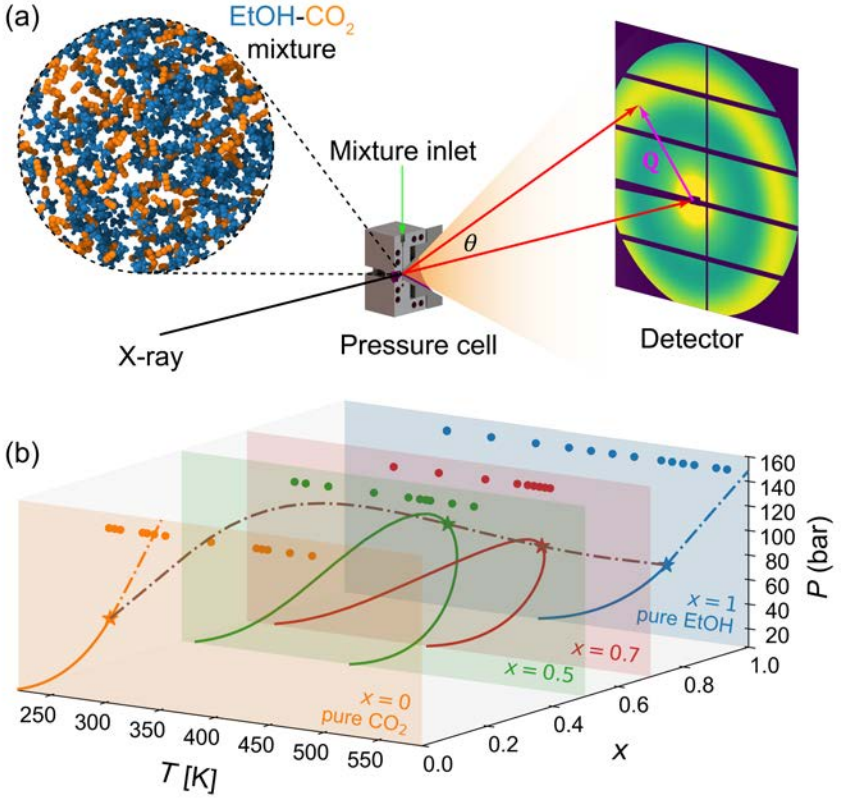

Figure 1: (a) Schematic of the X-ray scattering experiment. (b) Experimental conditions (dots) on the x-P-T phase diagram. Solid lines are liquid-vapor coexistence lines for single components and phase envelopes for mixtures. The brown dash-dotted line indicates the mixture critical locus. Dash-dotted lines for single components are Widom lines, which are defined as lines of maximum density fluctuations.

Large-scale MD simulations of EtOH-CO$_2$ mixtures with different mixing ratios were carried out using the LAMMPS software package[38] with a time step of 0.5 fs. The isothermal-isobaric ensemble (NPT) was employed by applying Nosé-Hoover thermostat and barostat with relaxation time scales of 50 fs and 500 fs, respectively. The system was initialized with a random distribution of EtOH and CO$_2$ molecules in a cubic box and run for 50 ps to reach equilibrium, during which density and potential energy were monitored. Equilibrium was confirmed once these quantities fluctuated around constant values. After equilibration, simulations were continued for an additional 450 ps for data collection. A total of 100,000 molecules were employed in each simulation, allowing for a minimum box size of ∼200 Å. Periodic boundary conditions were applied to the cubic simulation domain. The cut-off distance for short-range interactions was set to 17.5 Å. The long-range Coulomb interactions were computed using the particle–particle particle–mesh algorithm.[39] A rigid united-atom EtOH model, developed by Schnabel et al.[40] for reproducing vapor–liquid equilibria with low computational cost, was utilized in this work. For CO_2, the TraPPE force field[41] was applied, since it has been shown to accurately describe both microscopic structure[42] and thermodynamic response functions[43] of supercritical CO_2 (see SI for further details on the force-field evaluation).

Simulating the binary mixture of EtOH and CO_2 introduces an additional challenge in capturing the cross-species interactions between EtOH and CO_2 molecules. In pairwise additive potentials, two types of interactions are considered: (1) those between molecules of the same type, which are defined by the pure substance force fields, and (2) those between unlike molecules, which can be described using the modified Lorentz–Berthelot combining rule.[40] For two atoms, i and j, in two unlike molecules, the modified Lorentz–Berthelot combining rule is given by:

$$\sigma_{ij} = \frac{1}{2}(\sigma_i + \sigma_j), \tag{1a}$$

$$\epsilon_{ij} = \xi\sqrt{\epsilon_i\epsilon_j}. \tag{1b}$$

Here, σ and ϵ are the length and energy strength parameters in the Lennard-Jones interaction, and ξ is the binary interaction parameter that accounts for mixture effects. The standard Lorentz-Berthelot rule, where ξ is set to 1, has been shown to be insufficient for predicting unlike Lennard–Jones energy parameters in many binary mixtures.[40,44–46] Due to lack of prior experimental data for the isothermal liquid-vapor-equilibrium curves at high temperatures, we optimize the value of ξ by fitting the simulated structure factors to our experimental SAXS data for each composition. The optimized ξ values for the $x = 0.5$ and 0.7 mixtures are 0.95 and 0.90, respectively. Details about the optimization procedure and results for the ξ adjustment are provided in the SI. It is important to note that the Lorentz–Berthelot combining rule and its modified forms are inherently empirical and it is not evident that a single optimal ξ can universally describe all thermodynamic conditions.

Before computing the structure factor, we first reconstruct the full-atom EtOH geometry in each simulation snapshot by aligning the position and orientation of the hydroxyl group between the united-atom and full-atom geometries, ensuring that the reconstructed geometry captures the detailed intramolecular structure necessary for accurate scattering calculations. Then, the structure factor is obtained using a direct method[47] that calculates the Fourier transform of the electron density field by a single sum over all atomic positions (see SI for details of the structure factor calculation).

Figure 2 illustrates the measured structure factors from X-ray scattering experiments (dots) and simulated structure factors (lines). The mean unsigned errors (MUE) of the simulated structure factors with respect to the experimental data are provided in Table 1. The good agreement across experimental conditions encourages us to further analyze the microscopic structure of the EtOH-CO_2 mixtures over an extended range of temperatures from MD simulations, from 303 K to 630 K. The tabulated structure factors are provided in the SI.

Table 1: MUE of the structure factors from MD simulations compared to experimental data.

x	MUE (%)
0.0	6.0
0.5	4.1
0.7	4.0
1.0	4.6

The magnitude of density fluctuations in supercritical fluids is connected to the struc-

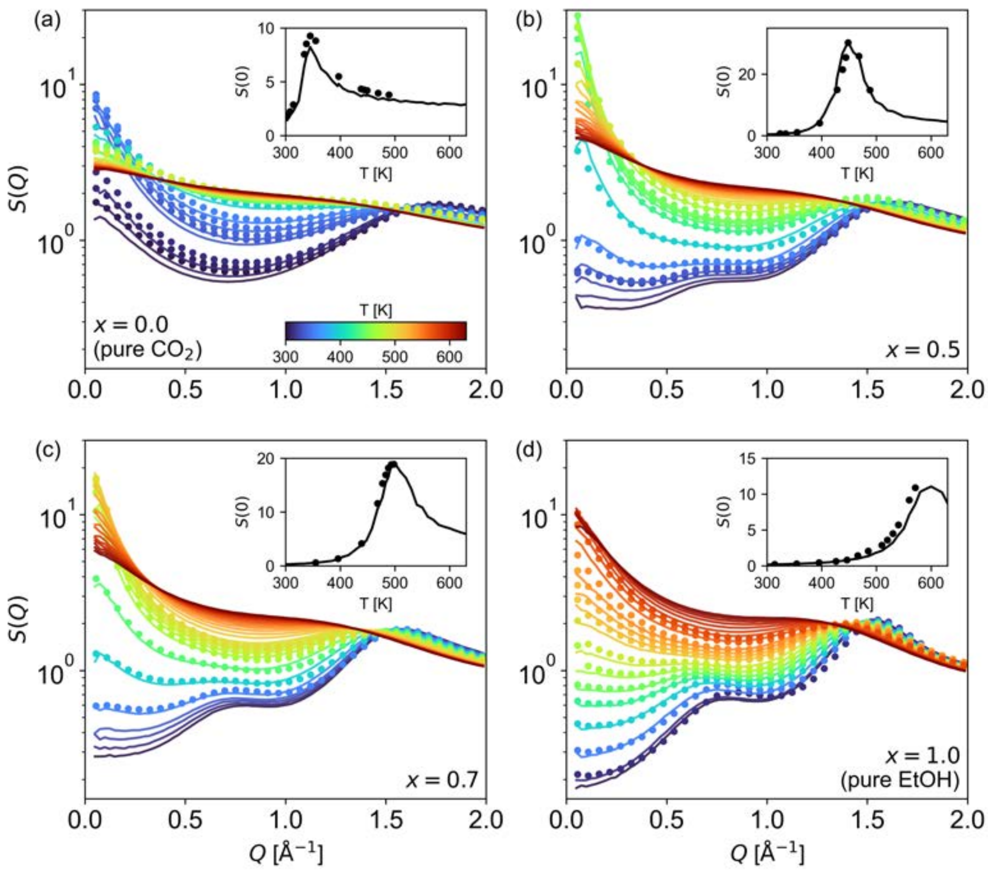

Figure 2: Structure factors of the mixtures of EtOH and CO_2 with EtOH mole fraction of (a) $x = 0.0$, (b) $x = 0.5$, (c) $x = 0.7$ and (d) $x = 1.0$ at different temperatures at $P = 147$ bar. Dots denote experimental results, and lines denote MD simulation results. The color scale for temperature is common to all panels. Insets show $S(0)$ at varying temperature.

ture factor at $Q = 0$.[48–50] We extrapolate $S(Q)$, from both SAXS measurement and MD simulations, to $Q = 0$ using a second order polynomial fit[51,52] to the low-Q region ($0.05 - 0.2$ Å^{-1}), shown as the insets in Figure 2. In this study, the Widom line is identified as the location of maximum $S(0)$, marking the strongest density heterogeneities and largest correlation length.[5,53,54] For $x = 0$, 0.5, 0.7, and 1.0, the Widom line temperatures are identified as 345, 448, 498, and 600 K, respectively. At the Widom temperatures of the mixtures ($x = 0.5$ and 0.7), while the pure fluids exhibit relatively homogeneous density distributions, upon mixing, the mixtures exhibit strong density heterogeneities. These results indicate that the low-Q structure of the mixture cannot be described as a linear superposition of the pure components. Based on these results, we hypothesize that EtOH and CO_2 are not fully miscible at the microscopic level, and the two components exhibit distinct phase behaviors at the molecular scale.

The potential micro-immiscibility of the mixture is supported by the persistence of medium-range spatial correlations among EtOH molecules. For pure EtOH at liquid-like state, the structure factor exhibits two peaks, as shown in Figure 2(d). The main peak is located at $Q \approx 1.5$ Å^{-1}, which represents the intermolecular correlations between neighboring EtOH molecules.[55] The inner peak is located at $Q \approx 0.75$ Å^{-1}, corresponding to a real-space distance of around 8.4 Å. Studies have shown that this medium-range correlation in alcohols originates from the correlations between OH groups,[55–57] signifying the formation of larger hydrogen-bonded supramolecular aggregates, which extend beyond the immediate first shell.[58,59] Our results show that this inner peak is preserved in the structure factor of the EtOH-CO_2 mixtures at lower temperature, as shown in Figure 2(b) and (c), indicating that EtOH molecules in the mixture retain a tendency to form self-associated aggregates, driven by hydrogen bonding, rather than dispersing evenly within the CO_2 matrix. Previous studies on the formation of hydrogen bonds between EtOH molecules in EtOH–CO_2 mixtures primarily demonstrated the existence of hydrogen bonds, either through NMR spectroscopy[33] or through molecular simulations.[28–30] However, these studies did not explicitly elucidate the structural organization resulting from these interactions. Our results provide direct experimental evidence that hydrogen bonding between EtOH molecules not only exists but also drives the formation of distinct supramolecular aggregates, characterized by persistent medium-range spatial correlations. This self-aggregation of EtOH molecules suggests that, despite the macroscopic miscibility of the mixture, the two components are not fully miscible at the molecular level, which could significantly alter solubility, transport properties, and reaction kinetics in practical applications.

Motivated by the complex behavior in the structure factor, we proceed to investigate the extent of micro-immiscibility and the phase behaviors of each component across different thermodynamic states. Since our MD simulations reproduce the experimental structure factors to good accuracy, we utilize the simulation data to separate the total structure factor into partial structure factors for the two components—namely EtOH-EtOH, CO_2-CO_2, and EtOH-CO_2 correlations, which provide insights into the local density correlations between different species. The partial structure factors are obtained by calculating the partial electron density fields of each component. Details of the computational procedure are provided in the SI.

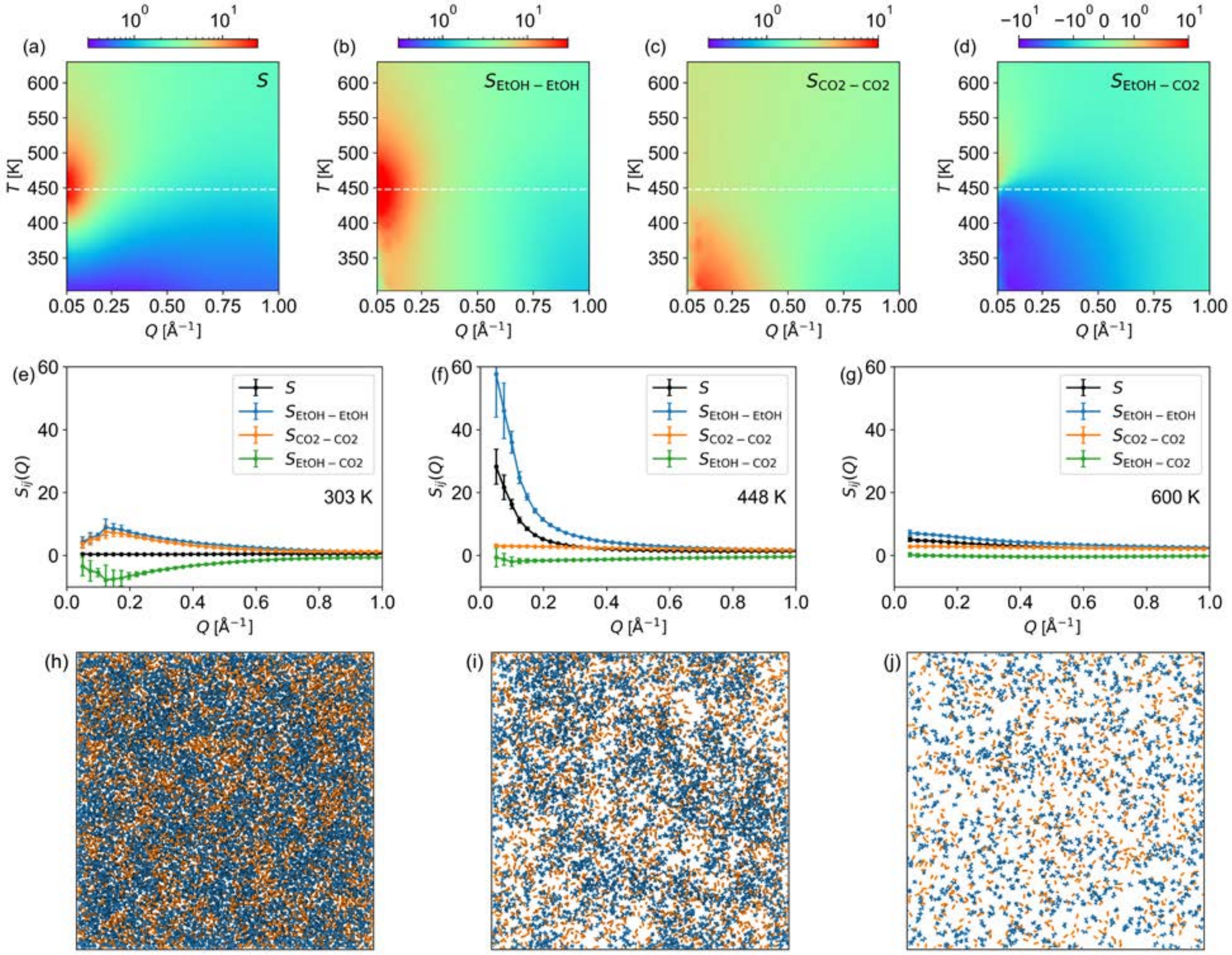

Figure 3: Total and partial structure factors of the $x = 0.5$ EtOH-CO_2 mixture for $Q < 1.0$ Å^{-1} region at varying temperature under constant pressure of 147 bar. The white dashed line represents the Widom line temperature of the mixture. (a-d) Contour plot of $S_{ij}(Q, T)$ for $i, j \in \{\mathrm{EtOH}, \mathrm{CO_2}\}$. Note that the colormap in (d) is in symmetric logarithmic scale since the cross-terms have both positive and negative values. (e-g) $S_{ij}(Q)$ at 303 K, 448 K and 600 K. (h-j) MD snapshots of the mixture at 303 K, 448 K and 600 K, with a viewing area of 200 × 200 Å^2 and a slice thickness of 20 Å. EtOH and CO_2 molecules are rendered in blue and orange, respectively.

We compute the partial structure factors for the $x = 0.5$ mixture with increasing temperature, $S_{ij}(Q,T)$, with $i, j \in \{\mathrm{EtOH}, \mathrm{CO_2}\}$. Figure 3 compares the total and partial structure factors. The Widom line temperature is illustrated as the dashed line. At lower temperatures, in the liquid-like state, while the mixture macroscopically appears homogeneous—evidenced by the absence of a low-Q peak in the total $S(Q)$—the partial structure factors reveal a more nuanced picture of local density organization, as shown in Figure 3(e). Both EtOH-EtOH and CO_2-CO_2 correlations exhibit broad peaks at $Q \approx 0.12$ Å^{-1}, indicating density heterogeneities within each component. Interestingly, the cross-term shows a negative peak in this region. The negativity of $S_{\mathrm{EtOH-CO2}}(Q)$ highlights an anti-correlation between EtOH and CO_2, meaning that the two components exhibit complementary spatial distributions, with one component's high-density regions coinciding with the other's low-density regions. Moreover, the presence of a peak implies that these heterogeneities are not random but structured and exhibit specific spatial characteristics driven by intermolecular interactions. The characteristic Q-value corresponds to a real-space separation distance of approximately 52 Å. Such a large distance indicates immiscibility at the microscopic level, which is further visualized in the MD snapshot shown in Figure 3(h). Regions of high EtOH density coincide with low CO_2 density, and vice versa, forming an intricate patchwork of locally enriched domains.

As the temperature approaches the Widom line, the total structure factor exhibits a pronounced increase in the low-Q region, indicating enhanced density fluctuations. The partial structure factors reveal a clear contrast in component-specific behavior: the low-Q signal of $S_{\mathrm{EtOH-EtOH}}(Q)$ increases [Figure 3(b,f)], signifying intensified EtOH clustering, while $S_{\mathrm{CO2-CO2}}(Q)$ flattens [Figure 3(c,f)], suggesting that CO_2 becomes more spatially uniform and gas-like, with reduced self-correlation. The cross-term $S_{\mathrm{EtOH-CO2}}(Q)$ is close to zero, indicating minimal cross-correlation between the two components. These results imply that near the Widom line, the mixture's local structure is dominated by liquid-like EtOH domains embedded within a more uniformly distributed CO_2 matrix. This is further visualized in the MD snapshot shown in Figure 3(i), which clearly shows EtOH clustering and dispersed CO_2 molecules.

As the temperature increases further into the gas-like regime, all partial structure factors flatten as shown in Figure 3(g), indicating a loss of long-range correlations. At this point, the mixture transitions to a more homogeneous state where both EtOH and CO_2 molecules are more uniformly distributed, as visualized in the MD snapshot in Figure 3(j).

These results indicate that although EtOH and CO_2 are classified as type-I mixture, meaning they are fully miscible and transition as a single phase on the macroscopic scale, they exhibit different phase behaviors at the microscopic scale. EtOH dominates the formation of local density heterogeneities, whereas CO_2 remains relatively evenly distributed at higher temperatures. Moreover, the analysis of anomalous thermophysical properties of the mixture near the Widom line are provided in the SI, where micro-heterogeneities are manifested by minimums in thermodynamics factors, peaks in density fluctuations, heat capacity and expansion coefficient, and large variations of self-diffusion coefficients.

The emergence of micro-immiscibility in the EtOH-CO_2 mixture is further elucidated by examining the clustering behaviors of the two components. We identify molecular clusters in the MD simulations using Hill's energy criterion,[60] which groups molecules into clusters based on physical principles of energy balance. This method has been widely used to study clustering in pure supercritical fluids.[6,61,62] In this study, we extend the approach to binary mixtures by considering cross-species interactions, see SI for details on the clustering algorithm. To balance computational efficiency with sufficient sampling, the number of molecules in the simulation is reduced to 20,000, while the simulation duration is extended to 4 ns, ensuring robust statistical characterization of the cluster structures.

For each cluster, we characterize its size, s, as the number of EtOH and CO_2 molecules it contains, i.e., $s = s_{\text{EtOH}} + s_{\text{CO2}}$. The number of clusters of every size, $N_c(s)$, is computed,

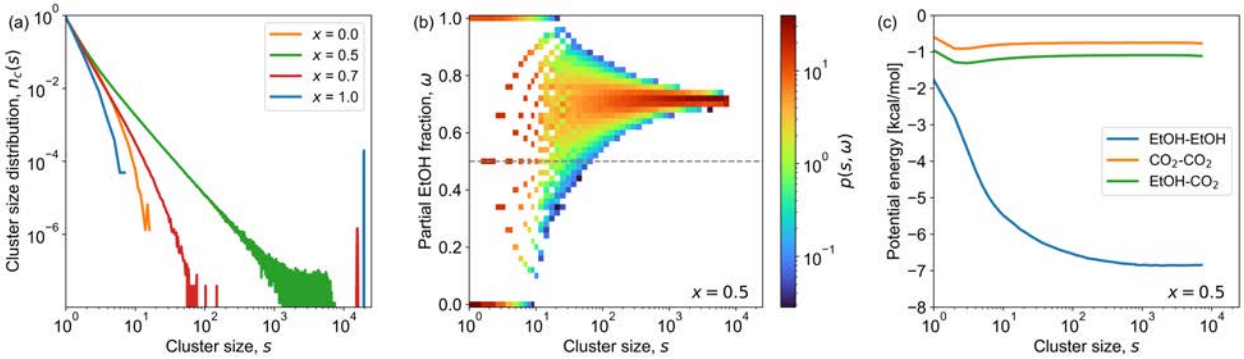

Figure 4: (a) Cluster size distributions for different EtOH fractions at 478 K and 147 bar. (b) Cluster distributions $p(s, \omega)$ on the partial EtOH fraction ω in clusters of size s for the $x = 0.5$ mixtures. The horizontal dashed lines denote the bulk EtOH fractions in the mixture. (c) EtOH-EtOH, CO_2-CO_2, and EtOH-CO_2 potential energies per EtOH or CO_2 molecule for clusters of different sizes in the $x = 0.5$ mixture.

and the cluster size distribution, $n_c(s)$, is then obtained as:

$$n_c(s) = \frac{N_c(s)}{\int_1^N N_c(s)\mathrm{d}s}, \tag{2}$$

Figure 4(a) compares $n_c(s)$ for mixtures with different EtOH fractions at 478 K, a temperature close to the Widom line of the $x = 0.5$ mixture. Pure CO_2 exhibits gas-like behavior with small, isolated clusters, while pure EtOH exhibits liquid-like clustering behavior, characterized by a single percolating cluster spanning the entire system. In contrast, the EtOH-CO_2 mixtures show a broader distribution of cluster sizes. Especially, the $x = 0.5$ mixture exhibits a power scaling of $n_c(s)$, which is consistent with the theory of percolation threshold[63] and indicates that the mixture exhibits structural heterogeneities across all length scales, with clusters of various sizes coexisting within the system. The $x = 0.7$ mixture, whose Widom line occurs at higher temperatures, exhibits liquid-like clustering behavior at 478 K.

To further investigate the molecular composition within clusters, we focus on the $x = 0.5$ mixture at 478 K, where the cluster size distribution is broad enough to facilitate a detailed analysis. We characterize the partial EtOH fraction as $\omega = s_{\mathrm{EtOH}}/(s_{\mathrm{EtOH}} + s_{\mathrm{CO2}})$, and compute its probability distribution, $p(s, \omega)$, in clusters of size s. This function satisfies the normalization conditions:

$$\iint p(s,\omega)n_c(s)\mathrm{d}\omega\mathrm{d}s = 1. \tag{3}$$

Figure 4(b) illustrates the partial fraction distribution $p(s,\omega)$ for the $x = 0.5$ mixtures at 478 K. The discontinuous distribution at small cluster sizes arises from the discrete molecular composition of clusters. A noticeable deviation from the bulk composition (denoted by the dashed line) indicates preferential segregation of EtOH and CO_2 within clusters. Monomers and dimers tend to be CO_2-rich, while larger clusters are more EtOH-rich. This result confirms that at the molecular level, EtOH and CO_2 do not mix ideally but instead form structurally distinct domains, exhibiting heterogeneities in both cluster size and local composition.

The underlying cause of this preferential segregation is examined by analyzing the intermolecular interactions within clusters. Figure 4(c) compares the EtOH-EtOH and EtOH-CO_2 potential energies per EtOH molecule, and CO_2-CO_2 potential energy per CO_2 molecule, for clusters of different sizes. Across all cluster sizes, EtOH molecules interact more strongly with each other than with CO_2, as indicated by the lower potential energy of EtOH-EtOH interactions compared to EtOH-CO_2 interactions. Moreover, the difference in interaction strength increases with cluster size, suggesting that larger clusters are more likely to be EtOH-rich. This trend arises from the stronger hydrogen bonding between EtOH molecules, which promotes their aggregation, while CO_2 molecules, lacking strong directional interactions, remain more weakly bound and dispersed throughout the system.

Another interesting observation from the EtOH fraction distribution in Figure 4(b) is that the partial EtOH fraction in larger clusters peaks at $\omega \approx 0.7$, rather than continuously increasing with EtOH content, as one might expect from the stronger EtOH-EtOH interaction, compared with the EtOH-CO_2 interaction. This indicates that simply adding more EtOH within a cluster does not necessarily result in the most thermodynamically stable configuration. Instead, an optimal cluster composition is achieved by balancing the favorable energetic interactions against the unfavorable reductions in entropy associated with increased molecular ordering. To validate this hypothesis, we proceed to quantify the variations in energy and entropy as a function of the partial EtOH fraction.

The specific internal energy, e, for a cluster of size s and partial EtOH fraction ω is defined as the average potential and kinetic energy per molecule in the cluster:

$$e(s,\omega) = \frac{1}{s}\left[\sum_{i=1}^{s\omega}\left(e_i^{\mathrm{kin}} + e_i^{\mathrm{pot}}\right)_{\mathrm{EtOH}} + \sum_{i=1}^{s(1-\omega)}\left(e_i^{\mathrm{kin}} + e_i^{\mathrm{pot}}\right)_{\mathrm{CO_2}}\right], \tag{4}$$

where e_i^{kin} and e_i^{pot} are the kinetic and potential energies of a molecule i within the cluster, and the subscripts EtOH and CO_2 denote the respective molecular species. The molecular potential energy is not restricted to the intra-cluster pairwise interactions but also includes the inter-cluster pairwise interactions, ensuring that the contribution of the cluster's interaction with its surrounding environment is accounted for. We compute the specific internal energy, $e(s,\omega)$, for clusters of different sizes and partial EtOH fractions, as shown in Figure 5(a). The specific internal energy decreases with increasing EtOH fraction, indicating that EtOH-rich clusters are energetically more favorable.

To assess the entropic contribution to the cluster stability, we consider the two-body excess entropy, which accounts for the dominant contribution to the configurational entropy of a fluid.[64,65] We compute the correlation function $g(r,\theta \mid s,\omega)$ for different cluster sizes and partial fractions, where r is the center-of-mass distance between two molecules, and θ is their relative orientation. In principle, the relative orientation between two rigid molecules is described by multiple angular degrees of freedom. However, constructing a full correlation function accounting for all possible relative orientations would be cumbersome.[66] Therefore, we adopt a simplified yet physically meaningful approach by defining a single orientational angle θ for each molecular pair type[66,67] [see SI for the detailed definitions and representative

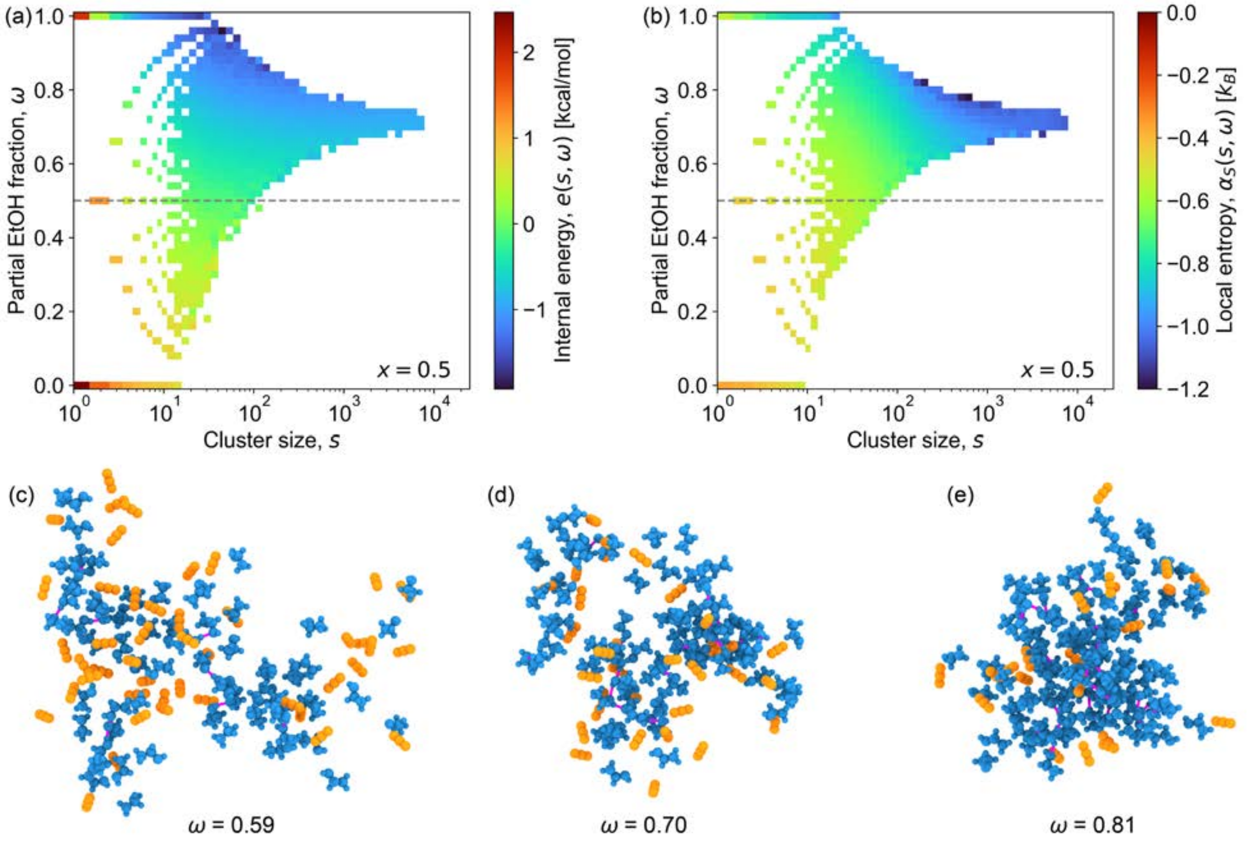

Figure 5: (a) Specific internal energy, $e(s, \omega)$, and (b) specific entropy fingerprint, $\alpha_S(s, \omega)$, for the $x = 0.5$ mixture at 478 K. (c-e) Cluster morphology. Representative snapshots of clusters of size $s = 109$ in the $x = 0.5$ mixture, with partial EtOH fraction ω of (c) 0.59, (d) 0.70 and (e) 0.81. EtOH and CO_2 molecules are rendered in blue and orange, respectively. Magenta lines represent hydrogen bonds.

results of $g(r, \theta \mid s, \omega)$]. Then the local entropy, $\alpha_S(s, \omega)$, is computed as:

$$\alpha_S(s, \omega) = -\pi \rho k_{\mathrm{B}} \int_0^{\infty} \int_0^{\pi} \left[g(r, \theta \mid s, \omega) \ln g(r, \theta \mid s, \omega) - g(r, \theta \mid s, \omega) + 1 \right] r^2 \sin\theta \mathrm{d}r \mathrm{d}\theta, \quad (5)$$

which includes both translational and orientational contributions. This approach has been applied in the studies of crystal nucleation and ordering transition.[66–68] To avoid confusion with the cluster size s, we denote the local entropy in this study as α_S.

As shown in Figure 5(b), the local entropy decreases with increasing EtOH fraction, indicating that EtOH-rich clusters become structurally more ordered. For clusters of the same size, the incorporation of additional EtOH molecules leads to the formation of a more rigid, hydrogen-bonded network, thus reducing the configurational freedom of the molecules. Figure 5(c-e) illustrate the morphological changes in clusters of size $s = 109$ at different partial EtOH fractions. As the EtOH fraction increases, the clusters become more compact and ordered, with EtOH molecules forming dense, interconnected networks. This observation is further confirmed by the network entropy and hydrogen bond analysis presented in SI. Consequently, although the increasing EtOH content lowers the internal energy, it simultaneously causes a loss in local entropy, which can counterbalance the energetic stabilization.

The tradeoff between energy and entropy may explain why the most stable cluster composition does not correspond to the highest possible EtOH fraction. Instead, an intermediate composition represents an optimal balance between energetic and entropic stabilization. Beyond this fraction, the diminishing entropy contribution outweighs the energetic gain, making further enrichment in EtOH less thermodynamically favorable. We acknowledge that the computed local entropy is a measure of the local structural order and does not represent the full configurational entropy. Therefore, a direct evaluation of the free energy distribution using the local entropy is not feasible. Nevertheless, the local entropy provides qualitative insight into the interplay between energy and entropy in determining the stability of molecular clusters.

The observation that the preferential composition of molecular clusters is larger than the bulk composition suggests that the system is not fully miscible at the molecular level, despite being classified as a type-I mixture. Previous experimental and theoretical studies have reported significant local composition enhancement in mixtures of supercritical CO_2 and alcohol cosolvents.[29,69,70] Specifically, when a polar solute is introduced into a supercritical alcohol–CO_2 solvent mixture, the local mole fraction of the alcohol cosolvent in the vicinity of the polar solute molecules is markedly increased compared to its bulk composition. Such local enrichment of the alcohol cosolvent is directly attributed to the formation of alcohol-rich supramolecular aggregates within the mixture.[29,71] These locally enhanced polar domains serve as preferential solvation sites, favoring the dissolution of polar solutes.

Although prior interpretations linking local composition enhancement to aggregate formation were largely qualitative, our current findings provide direct structural evidence of such alcohol-rich aggregation phenomena at the microscopic scale. Our structure factor and clustering analyses explicitly demonstrate that EtOH molecules indeed form distinct, structurally ordered aggregates with a preferred local composition driven by a balance between energetic stabilization and entropic loss, confirming that local aggregation significantly affects the microscopic mixing behavior.

In summary, SAXS experiments were conducted to investigate the microscopic structure of supercritical EtOH-CO_2 mixtures at varying thermodynamic states. These experimental results were compared with MD simulations using optimized force field parameters to provide detailed insights into the molecular interactions and phase behaviors of the mixture. The structure factor of the mixture was found to exhibit complex behavior, indicating that the interactions between EtOH and CO_2 in the mixture give rise to unique structural features that cannot be captured by a mere additive combination of the pure component behaviors. The persistence of medium-range spatial correlations among EtOH molecules was observed in the mixture, indicating the formation of hydrogen-bonded supramolecular aggregates. The partial structure factors revealed that EtOH and CO_2 exhibit distinct local structuring, with EtOH forming pronounced clusters due to strong hydrogen bonding, while CO_2 shows more uniform distribution. The emergence of micro-immiscibility was further supported by the cluster analysis, which showed that EtOH and CO_2 form structurally distinct domains within the mixture. The preferential composition of molecular clusters was found to be larger than the bulk composition, indicating that the system is not fully miscible at the molecular level. The formation of stable supramolecular aggregates was shown to be dependent on a balance between energetic stabilization and entropy loss.

Our findings provide new understanding of type-I mixture characterization, showing that in macroscopically miscible systems, the components can retain distinct microstructural identities. These insights are crucial for controlling and optimizing industrial processes, such as supercritical extraction and material synthesis, where efficiency strongly depends on microscopic structuring.

Acknowledgement

This work was supported by the U.S. Department of Energy, Office of Science with award number DE-SC0022222. The authors are grateful for the resources at the National Energy Research Scientific Computing Center and Stanford Research Computing Center that were utilized for this work. Use of the Stanford Synchrotron Radiation Lightsource, SLAC National Accelerator Laboratory, is supported by the U.S. Department of Energy, Office of Science, Office of Basic Energy Sciences under Contract No. DE-AC02-76SF00515. The Pilatus detector at beamline 4-2 at SSRL was funded under National Institutes of Health Grant S10OD021512. The SSRL Structural Molecular Biology Program is supported by the DOE Office of Biological and Environmental Research, and by the National Institutes of Health, National Institute of General Medical Sciences (P30GM133894). The content of this publication is solely the responsibility of the authors and does not necessarily represent the official views of NIGMS or NIH.

Supporting Information Available

The following files are available free of charge.

- supporting_info.pdf: Experimental and computational details, including sample preparation, structure factor calculation, force fields in MD simulations, anomalous properties near the Widom line at the system level, cluster identification, relative orientation definitions, network entropy and hydrogen bond distributions on cluster size and partial EtOH fraction.
- structure_factor.zip: Data for experimental structure factors of the EtOH-CO_2 mix-

tures.

References

(1) Aymonier, C.; Loppinet-Serani, A.; Reverón, H.; Garrabos, Y.; Cansell, F. Review of Supercritical Fluids in Inorganic Materials Science. *J. Supercrit. Fluids* **2006**, *38*, 242–251.

(2) Benson, S. M.; Cole, D. R. CO_2 Sequestration in Deep Sedimentary Formations. *Elements* **2008**, *4*, 325–331.

(3) Adschiri, T.; Yoko, A. Supercritical Fluids for Nanotechnology. *J. Supercrit. Fluids* **2018**, *134*, 167–175.

(4) Cockrell, C.; Brazhkin, V. V.; Trachenko, K. Transition in the Supercritical State of Matter: Review of Experimental Evidence. *Phys. Rep.* **2021**, *941*, 1–27.

(5) Shagurin, A.; Miannay, F. A.; Kiselev, M. G.; Jedlovszky, P.; Affouard, F.; Idrissi, A. Widom Line in Supercritical Water in Terms of Changes in Local Structure: Theoretical Perspective. *J. Phys. Chem. Lett.* **2024**, *15*, 5831–5837.

(6) Simeski, F.; Ihme, M. Supercritical Fluids Behave as Complex Networks. *Nat. Commun.* **2023**, *14*, 1996.

(7) Araus, K. A.; Casado, V.; del Valle, J. M.; Robert, P. S.; de la Fuente, J. C. Cosolvent Effect of Ethanol on the Solubility of Lutein in Supercritical Carbon Dioxide. *J. Supercrit. Fluids.* **2019**, *143*, 205–210.

(8) Al-Hamimi, S.; Abellan Mayoral, A.; Cunico, L. P.; Turner, C. Carbon Dioxide Expanded Ethanol Extraction: Solubility and Extraction Kinetics of α-Pinene and Cis-Verbenol. *Anal. Chem.* **2016**, *88*, 4336–4345.

(9) Özbakır, Y.; Erkey, C. Experimental and Theoretical Investigation of Supercritical Drying of Silica Alcogels. *J. Supercrit. Fluids.* **2015**, *98*, 153–166.

(10) Subra-Paternault, P.; Harscoat-Schiavo, C.; Savoire, R.; Brun, M.; Velasco, J.; Ruiz-Mendez, V. Utilization of Pressurized CO_2, Pressurized Ethanol and CO_2-expanded Ethanol Mixtures for de-Oiling Spent Bleaching Earths. *J. Supercrit. Fluids.* **2019**, *149*, 42–53.

(11) Santos, C. I. A. V.; Barros, M. C. F.; Ribeiro, A. C. F. Diffusion of Ethanol in Supercritical Carbon Dioxide—Investigation of scCO_2-cosolvent Mixtures Used in Pharmaceutical Applications. *Processes* **2022**, *10*, 660.

(12) Scott, R. L.; van Konynenburg, P. H. Static Properties of Solutions. Van Der Waals and Related Models for Hydrocarbon Mixtures. *Discuss. Faraday Soc.* **1970**, *49*, 87–97.

(13) van Konynenburg, P. H.; Scott, R. L.; Rowlinson, J. S. Critical Lines and Phase Equilibria in Binary van Der Waals Mixtures. *Philos. Trans. R. Soc. A* **1980**, *298*, 495–540.

(14) Raju, M.; Banuti, D. T.; Ma, P. C.; Ihme, M. Widom Lines in Binary Mixtures of Supercritical Fluids. *Sci. Rep.* **2017**, *7*, 3027.

(15) Rowlinson, J. S. *Liquids and Liquid Mixtures*, 3rd ed.; Butterworths Monographs in Chemistry; Butterworth Scientific: London, 1982.

(16) Sirignano, W. A.; Delplanque, J.-P. Transcritical Vaporization of Liquid Fuels and Propellants. *J. Propuls. Power* **1999**, *15*, 896–902.

(17) Cismondi, M.; Michelsen, M. L. Global Phase Equilibrium Calculations: Critical Lines, Critical End Points and Liquid–Liquid–Vapour Equilibrium in Binary Mixtures. *J. Supercrit. Fluids.* **2007**, *39*, 287–295.

(18) Monteiro, M. F.; Moura-Neto, M. H.; Pereira, C. G.; Chiavone-Filho, O. Description of

Phase Equilibrium and Volumetric Properties for CO_2+water and CO_2+ethanol Using the CPA Equation of State. *J. Supercrit. Fluids.* **2020**, *161*, 104841.

(19) Secuianu, C.; Feroiu, V.; Geană, D. Phase Behavior for Carbon Dioxide + Ethanol System: Experimental Measurements and Modeling with a Cubic Equation of State. *J. Supercrit. Fluids.* **2008**, *47*, 109–116.

(20) Milovanović, M. R.; Zarić, S. D. New Aspects of Alcohol–Alcohol and Alcohol–Water Interactions: Crystallographic and Quantum Chemical Studies of Antiparallel O–H/O–H Interactions. *J. Phys. Chem. Lett.* **2024**, *15*, 1294–1304.

(21) Shagurin, A.; Miannay, F. A.; Kiselev, M. G.; Jedlovszky, P.; Correia, N. T.; Affouard, F.; Idrissi, A. Impact of Intermolecular Forces on Structural Changes and Local Density Fluctuations of CO_2 in Liquid and Supercritical Phases. *J. Phys. Chem. Lett.* **2025**, *16*, 2778–2784.

(22) Muhunthan, P.; Paredes Mellone, O.; Kroll, T.; Sokaras, D.; Ihme, M. The Local Electronic Structure of Supercritical CO_2 from X-ray Raman Spectroscopy and Atomistic-Scale Modeling. *J. Phys. Chem. Lett.* **2023**, *14*, 4955–4961.

(23) Krishna, R.; van Baten, J. M. Describing Diffusion in Fluid Mixtures at Elevated Pressures by Combining the Maxwell–Stefan Formulation with an Equation of State. *Chem. Eng. Sci.* **2016**, *153*, 174–187.

(24) Guevara-Carrion, G.; Ancherbak, S.; Mialdun, A.; Vrabec, J.; Shevtsova, V. Diffusion of Methane in Supercritical Carbon Dioxide across the Widom Line. *Sci. Rep.* **2019**, *9*, 8466.

(25) Chatwell, R. S.; Guevara-Carrion, G.; Gaponenko, Y.; Shevtsova, V.; Vrabec, J. Diffusion of the Carbon Dioxide–Ethanol Mixture in the Extended Critical Region. *Phys. Chem. Chem. Phys.* **2021**, *23*, 3106–3115.

(26) Saric, D.; Guevara-Carrion, G.; Gaponenko, Y.; Shevtsova, V.; Vrabec, J. Diffusion of Hydrocarbons Diluted in Supercritical Carbon Dioxide. *Sci Rep* **2023**, *13*, 16107.

(27) Debenedetti, P. G. Clustering in Dilute, Binary Supercritical Mixtures: A Fluctuation Analysis. *Chem. Eng. Sci.* **1987**, *42*, 2203–2212.

(28) Skarmoutsos, I.; Guardia, E.; Samios, J. Hydrogen Bond, Electron Donor-Acceptor Dimer, and Residence Dynamics in Supercritical CO_2-ethanol Mixtures and the Effect of Hydrogen Bonding on Single Reorientational and Translational Dynamics: A Molecular Dynamics Simulation Study. *J. Chem. Phys.* **2010**, *133*, 014504.

(29) Skarmoutsos, I.; Dellis, D.; Samios, J. Investigation of the Local Composition Enhancement and Related Dynamics in Supercritical CO_2-cosolvent Mixtures via Computer Simulation: The Case of Ethanol in CO_2. *J. Chem. Phys.* **2007**, *126*, 224503.

(30) Xu, W.; Yang, J.; Hu, Y. Microscopic Structure and Interaction Analysis for Supercritical Carbon Dioxide-ethanol Mixtures: A Monte Carlo Simulation Study. *J. Phys. Chem. B* **2009**, *113*, 4781–4789.

(31) Saharay, M.; Balasubramanian, S. Electron Donor-acceptor Interactions in ethanol-CO_2 Mixtures: An Ab Initio Molecular Dynamics Study of Supercritical Carbon Dioxide. *J. Phys. Chem. B* **2006**, *110*, 3782–3790.

(32) Cabaço, M. I.; Danten, Y.; Tassaing, T.; Longelin, S.; Besnard, M. Raman Spectroscopy of CO_2–Acetone and CO_2–Ethanol Complexes. *Chem. Phys. Lett.* **2005**, *413*, 258–262.

(33) Reiser, S.; McCann, N.; Horsch, M.; Hasse, H. Hydrogen Bonding of Ethanol in Supercritical Mixtures with CO_2 by 1H NMR Spectroscopy and Molecular Simulation. *J. Supercrit. Fluids.* **2012**, *68*, 94–103.

(34) Mareev, E.; Semenov, T.; Lazarev, A.; Minaev, N.; Sviridov, A.; Potemkin, F.; Gor-

dienko, V. Optical Diagnostics of Supercritical CO_2 and CO_2-ethanol Mixture in the Widom Delta. *Molecules* **2020**, *25*, 5424.

(35) Mareev, E. I.; Sviridov, A. P.; Gordienko, V. M. The Anomalous Behavior of Thermodynamic Parameters in the Three Widom Deltas of Carbon Dioxide-Ethanol Mixture. *Int. J. Mol. Sci.* **2021**, *22*, 9813.

(36) Smolsky, I. L.; Liu, P.; Niebuhr, M.; Ito, K.; Weiss, T. M.; Tsuruta, H. Biological Small-Angle X-ray Scattering Facility at the Stanford Synchrotron Radiation Laboratory. *J. Appl. Cryst.* **2007**, *40*, s453–s458.

(37) Muhunthan, P.; Li, H.; Vignat, G.; Toro, E. R.; Younes, K.; Sun, Y.; Sokaras, D.; Weiss, T.; Rajkovic, I.; Osaka, T. et al. A Versatile Pressure-Cell Design for Studying Ultrafast Molecular-Dynamics in Supercritical Fluids Using Coherent Multi-Pulse X-ray Scattering. *Rev. Sci. Instrum.* **2024**, *95*, 013901.

(38) Thompson, A. P.; Aktulga, H. M.; Berger, R.; Bolintineanu, D. S.; Brown, W. M.; Crozier, P. S.; in 't Veld, P. J.; Kohlmeyer, A.; Moore, S. G.; Nguyen, T. D. et al. LAMMPS — a Flexible Simulation Tool for Particle-Based Materials Modeling at the Atomic, Meso, and Continuum Scales. *Comput. Phys. Commun.* **2022**, *271*, 108171.

(39) Hockney, R. W.; Eastwood, J. W. *Computer Simulation Using Particles*; Taylor & Francis: New York, 1988.

(40) Schnabel, T.; Vrabec, J.; Hasse, H. Henry's Law Constants of Methane, Nitrogen, Oxygen and Carbon Dioxide in Ethanol from 273 to 498 K: Prediction from Molecular Simulation. *Fluid Ph. Equilib.* **2005**, *233*, 134–143.

(41) Potoff, J. J.; Siepmann, J. I. Vapor–Liquid Equilibria of Mixtures Containing Alkanes, Carbon Dioxide, and Nitrogen. *AIChE J.* **2001**, *47*, 1676–1682.

(42) Majumdar, A.; Li, H.; Muhunthan, P.; Späh, A.; Song, S.; Sun, Y.; Chollet, M.; Sokaras, D.; Zhu, D.; Ihme, M. Direct Observation of Ultrafast Cluster Dynamics in Supercritical Carbon Dioxide Using X-ray Photon Correlation Spectroscopy. *Nat. Commun.* **2024**, *15*, 10540.

(43) Aimoli, C. G.; Maginn, E. J.; Abreu, C. R. A. Force Field Comparison and Thermodynamic Property Calculation of Supercritical CO_2 and CH_4 Using Molecular Dynamics Simulations. *Fluid Ph. Equilib.* **2014**, *368*, 80–90.

(44) Schnabel, T.; Vrabec, J.; Hasse, H. Unlike Lennard–Jones Parameters for Vapor–Liquid Equilibria. *J. Mol. Liq.* **2007**, *135*, 170–178.

(45) Vrabec, J.; Stoll, J.; Hasse, H. Molecular Models of Unlike Interactions in Fluid Mixtures. *Mol. Simul.* **2005**, *31*, 215–221.

(46) Stoll, J.; Vrabec, J.; Hasse, H. Vapor–Liquid Equilibria of Mixtures Containing Nitrogen, Oxygen, Carbon Dioxide, and Ethane. *AIChE J.* **2003**, *49*, 2187–2198.

(47) Mohanty, S.; Cooper, C. B.; Wang, H.; Liang, M.; Cai, W. Computational Approaches to Model X-ray Photon Correlation Spectroscopy from Molecular Dynamics. *Modelling Simul. Mater. Sci. Eng.* **2022**, *30*, 075004.

(48) Nishikawa, K.; Tanaka, I. Correlation Lengths and Density Fluctuations in Supercritical States of Carbon Dioxide. *Chem. Phys. Lett.* **1995**, *244*, 149–152.

(49) Morita, T.; Kusano, K.; Ochiai, H.; Saitow, K.-i.; Nishikawa, K. Study of Inhomogeneity of Supercritical Water by Small-Angle X-ray Scattering. *J. Chem. Phys.* **2000**, *112*, 4203–4211.

(50) Nishikawa, K. The Solution Chemistry of Mixing States Probed via Fluctuations: A Direct Description of Inhomogeneity in Mixing. *Bulletin of the Chemical Society of Japan* **2021**, *94*, 2170–2186.

(51) Huang, C.; Wikfeldt, K. T.; Tokushima, T.; Nordlund, D.; Harada, Y.; Bergmann, U.; Niebuhr, M.; Weiss, T. M.; Horikawa, Y.; Leetmaa, M. et al. The Inhomogeneous Structure of Water at Ambient Conditions. *Proc. Natl. Acad. Sci. U.S.A.* **2009**, *106*, 15214–15218.

(52) Clark, G. N. I.; Hura, G. L.; Teixeira, J.; Soper, A. K.; Head-Gordon, T. Small-Angle Scattering and the Structure of Ambient Liquid Water. *Proc. Natl. Acad. Sci. U.S.A.* **2010**, *107*, 14003–14007.

(53) Simeoni, G. G.; Bryk, T.; Gorelli, F. A.; Krisch, M.; Ruocco, G.; Santoro, M.; Scopigno, T. The Widom Line as the Crossover between Liquid-like and Gas-like Behaviour in Supercritical Fluids. *Nat. Phys.* **2010**, *6*, 503–507.

(54) Ha, M. Y.; Yoon, T. J.; Tlusty, T.; Jho, Y.; Lee, W. B. Widom Delta of Supercritical Gas–Liquid Coexistence. *J. Phys. Chem. Lett.* **2018**, *9*, 1734–1738.

(55) Tomšič, M.; Jamnik, A.; Fritz-Popovski, G.; Glatter, O.; Vlček, L. Structural Properties of Pure Simple Alcohols from Ethanol, Propanol, Butanol, Pentanol, to Hexanol: Comparing Monte Carlo Simulations with Experimental SAXS Data. *J. Phys. Chem. B* **2007**, *111*, 1738–1751.

(56) Böhmer, R.; Gainaru, C.; Richert, R. Structure and Dynamics of Monohydroxy Alcohols—Milestones towards Their Microscopic Understanding, 100 Years after Debye. *Phys. Rep.* **2014**, *545*, 125–195.

(57) Vahvaselkä, K. S.; Serimaa, R.; Torkkeli, M. Determination of Liquid Structures of the Primary Alcohols Methanol, Ethanol, 1-Propanol, 1-Butanol and 1-Octanol by X-ray Scattering. *J. Appl. Cryst.* **1995**, *28*, 189–195.

(58) Nowok, A.; Dulski, M.; Grelska, J.; Szeremeta, A. Z.; Jurkiewicz, K.; Grzybowska, K.; Musiał, M.; Pawlus, S. Phenyl Ring: A Steric Hindrance or a Source of Different

Hydrogen Bonding Patterns in Self-Organizing Systems? *J. Phys. Chem. Lett.* **2021**, *12*, 2142–2147.

(59) Požar, M.; Perera, A. On the Existence of a Scattering Pre-Peak in the Mono-Ols and Diols. *Chem. Phys. Lett.* **2017**, *671*, 37–43.

(60) Hill, T. L. Molecular Clusters in Imperfect Gases. *J. Chem. Phys.* **1955**, *23*, 617–622.

(61) Campi, X.; Krivine, H.; Sator, N. Percolation Line of Self-Bound Clusters in Supercritical Fluids. *Physica A Stat. Mech. Appl.* **2001**, *296*, 24–30.

(62) Fan, J.; Ly, N.; Ihme, M. Heterogeneous Cluster Energetics and Nonlinear Thermodynamic Response in Supercritical Fluids. *Phys. Rev. Lett.* **2024**, *133*, 248001.

(63) Sahimi, M. *Applications of Percolation Theory*; Applied Mathematical Sciences; Springer International Publishing: Cham, 2023; Vol. 213.

(64) Baranyai, A.; Evans, D. J. Three-Particle Contribution to the Configurational Entropy of Simple Fluids. *Phys. Rev. A* **1990**, *42*, 849–857.

(65) Giuffré, E.; Prestipino, S.; Saija, F.; Saitta, A. M.; Giaquinta, P. V. Entropy from Correlations in TIP4P Water. *J. Chem. Theory Comput.* **2010**, *6*, 625–636.

(66) Piaggi, P. M.; Parrinello, M. Predicting Polymorphism in Molecular Crystals Using Orientational Entropy. *Proc. Natl. Acad. Sci. U.S.A.* **2018**, *115*, 10251–10256.

(67) Zou, Z.; Beyerle, E. R.; Tsai, S.-T.; Tiwary, P. Driving and Characterizing Nucleation of Urea and Glycine Polymorphs in Water. *Proc. Natl. Acad. Sci. U.S.A.* **2023**, *120*, e2216099120.

(68) Song, H.; Vogt-Maranto, L.; Wiscons, R.; Matzger, A. J.; Tuckerman, M. E. Generating Cocrystal Polymorphs with Information Entropy Driven by Molecular Dynamics-Based Enhanced Sampling. *J. Phys. Chem. Lett.* **2020**, *11*, 9751–9758.

(69) Chen, J.; Shen, D.; Wu, W.; Han, B.; Wang, B.; Sun, D. Solvatochromic Behavior of Phenol Blue in CO_2+ethanol and CO_2+n-pentane Mixtures in the Critical Region and Local Composition Enhancement. *J. Chem. Phys.* **2005**, *122*, 204508.

(70) Kim, S.; Johnston, K. P. Clustering in Supercritical Fluid Mixtures. *AIChE J.* **1987**, *33*, 1603–1611.

(71) Tassaing, T.; Lalanne, P.; Rey, S.; Cansell, F.; Besnard, M. Spectroscopic Study of the Polystyrene//CO2/Ethanol System. *Ind. Eng. Chem. Res.* **2000**, *39*, 4470–4475.

Supporting Information for

Supercritical ethanol–CO_2 mixtures exhibit microscopic immiscibility: A combined study using X-ray scattering and molecular dynamics simulations

Jingcun Fan[1,*], Taekeun Yoon[1], Guillaume Vignat[1], Haoyuan Li[1], Khaled Younes[1], Arijit Majumdar[1], Priyanka Muhunthan[1], Dimosthenis Sokaras[2], Thomas Weiss[2], Ivan Rajkovic[2], and Matthias Ihme[1,2,3,*]

[1]Department of Mechanical Engineering, Stanford University, Stanford, CA, 94305, USA
[2]SLAC National Accelerator Laboratory, Menlo Park, CA, 94025, USA
[3]Department of Energy Science and Engineering, Stanford University, Stanford, CA, 94305, USA
[*]jcfan@stanford.edu, mihme@stanford.edu

Contents

1 Sample preparation

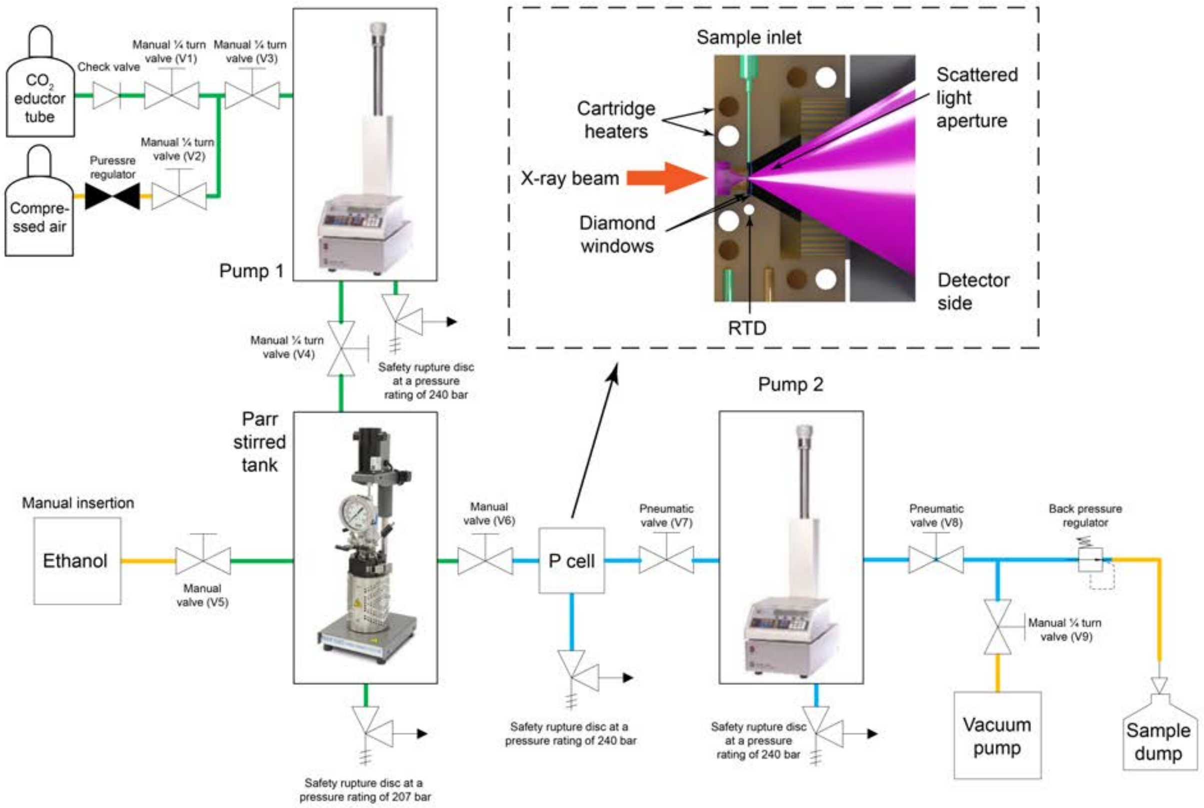

Figure S1: EtOH-CO$_2$ mixture preparation setup. Inset in the dashed rectangle is the cut view of the pressure cell [1].

In this section, we discuss our procedure to prepare and maintain the mixture sample. The flow diagram of the sample system is shown in Figure S1. A predetermined volume of EtOH ($\geq$ 99.5 % purity, ACS reagent grade, 200 proof, Sigma-Aldrich) is measured and injected into a buffer vessel (5500 HP Compact Reactors, 600 mL, Parr Instrument) using a manual glass syringe. Liquid CO$_2$ (99.9 % purity) from a cylinder with an eductor tube is injected into the Parr reactor using a syringe pump (DX100, Teledyne ISCO), which, combined with pressure and temperature measurements, is used as a metering device to calculate the mass of injected CO$_2$. Once the desired EtOH-CO$_2$ mole ratio is reached, the syringe pump is used to pressurize the mixture to 147 bar, ensuring miscibility in the liquid phase. A stirrer in the buffer vessel aids in quickly achieving a well-mixed mixture, and two synchronized syringe pumps (DX100 and DM100, Teledyne ISCO) are used to maintain consistent mixing and delivery of the sample to a pressure cell [1]. The sample is constantly circulated between the two syringe pumps to further ensure homogeneity. The synchronized operation of the syringe pumps prevents pressure oscillations, ensuring that the sample remains in a single phase throughout the experiment. The sample is heated to the target temperature within the pressure cell using electric cartridge heaters. A PID temperature controller (Lakeshore Cryotronics) is used to maintain temperature stability with a Platinum-RTD sensor embedded in the pressure cell acting as the temperature reference. The sample temperature is measured with K-type thermocouples inside the pressure cell. The experimental thermodynamic conditions are summarized in Tabel S1.

Our experimental thermodynamic conditions are chosen based on the phase diagram of the mixture as shown in Figure S2. For each fixed composition, the solid line represents the coexistence curve, i.e., the

Table S1: Thermodynamic conditions in the SAXS experiments

x	P (bar)	T (K)
0.0	147	303, 308, 314, 334, 338, 345, 355, 397, 438, 443, 449, 469, 489
0.5		324, 334, 355, 396, 428, 438, 444, 448, 468, 488
0.7		355, 396, 439, 468, 477, 483, 488, 493, 498
1.0		314, 354, 395, 426, 446, 466, 485, 510, 520, 530, 540, 560, 571

phase envelope. The locus of critical points for varying compositions is represented as dotted line. Our chosen pressure of P = 147 bar lies above all the critical pressures for all studied compositions (highlighted in the figure), and well outside the two-phase regions delineated by the coexistence envelopes, ensuring the system remains in the supercritical regime throughout the entire temperature range.

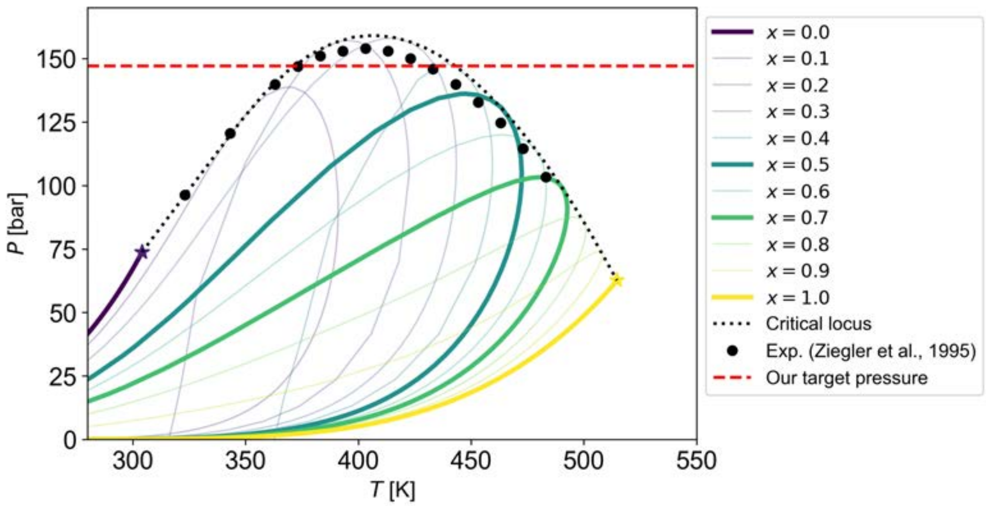

Figure S2: Phase diagram of the EtOH-CO$_2$ mixture projected on the $P-T$ plane. Solid lines are phase coexistence curves for each composition via the Peng-Robinson equation of state. Experimental compositions (x = 0, 0.5, 0.7, and 1.0) are highlighted. The dotted line represents the line of critical points for all compositions. Black dot symbols are critical points measured from experiments [2].

To evaluate the accuracy of temperature control in the SAXS experiments, we assess density fluctuations of pure CO$_2$ by extrapolating the measured structure factor to Q = 0. This is achieved using a second-order polynomial fit over the low-Q range (0.05–0.2 Å^{-1}) [3, 4]. Details of the structure factor calculation are provided in the next section. The extracted $S(0)$ values are compared to reference density fluctuations from NIST, given by $\rho k_{\mathrm{B}} T \kappa_T$ [4], where ρ is the number density, k_{B} is Boltzmann's constant, and κ_T is the isothermal compressibility. As shown in Figure S3, the normalized density fluctuations from SAXS measurements agree well with the NIST values. Notably, the temperature corresponding to the maximum fluctuation closely matches the NIST prediction, confirming the reliability of the experimental temperature measurements. In this study, the NIST reference data are obtained using the open-source thermophysical property library CoolProp [5] which implements the same high-accuracy Helmholtz energy equations of state for CO$_2$ [6] and EtOH [7] as NIST REFPROP 10.0 [8].

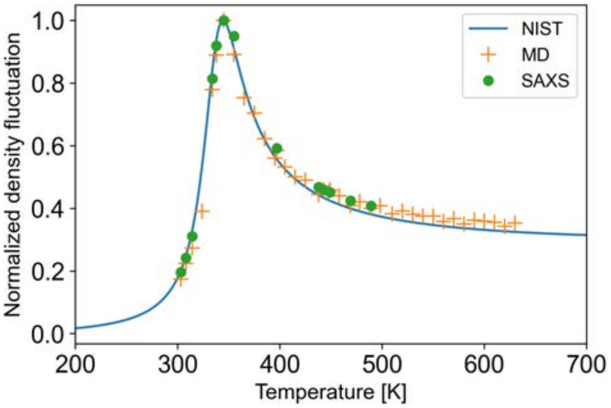

Figure S3: Normalized density fluctuations for pure CO_2. The solid line represent NIST values using $\rho k_{\mathrm{B}}\kappa_T$. Markers represent MD and SAXS results using $S(0)$.

2 Structure factor calculation

Under the independent atom approximation [9], the X-ray scattering intensity, $I(\mathbf{Q})$, for a multi-atomic system can be written as

$$I(\mathbf{Q}) = \sum_{n=1}^{N_a}\sum_{m=1}^{N_a} f_n(\mathbf{Q}) f_m(\mathbf{Q}) \mathrm{e}^{\mathrm{i}\mathbf{Q}\cdot(\mathbf{r}_n-\mathbf{r}_m)}, \tag{S1}$$

where n and m denote two atoms, $f_n(\mathbf{Q})$ is the atomic form factor, $\mathbf{r}_n$ is the position of atom n, and N_a is the number of atoms.

The structure factor, $S(\mathbf{Q})$, is defined as

$$S(\mathbf{Q}) = \frac{I(\mathbf{Q})}{\sum_{n=1}^{N_a} f_n^2(\mathbf{Q})}. \tag{S2}$$

For the mixture of EtOH and CO_2, the denominator in Eq. S2 can be written as

$$\sum_{n=1}^{N_a} f_n^2(\mathbf{Q}) = N f_{\text{mix}}^2(\mathbf{Q}), \tag{S3}$$

where N is the number of molecules and $f_{\text{mix}}(\mathbf{Q})$ is the molecular form factor of the mixture which is defined as

$$f_{\text{mix}}(\mathbf{Q}) = \left[x f_{\text{EtOH}}^2(\mathbf{Q}) + (1-x) f_{\text{CO2}}^2(\mathbf{Q})\right]^{1/2}, \tag{S4}$$

where x is the mole fraction of EtOH in the mixture, and $f_{\text{EtOH}}(\mathbf{Q})$ and $f_{\text{CO2}}(\mathbf{Q})$ are the molecular form factors of EtOH and CO_2, respectively, and are defined as

$$f_{\text{EtOH}}(\mathbf{Q}) = \left[f_{\text{C}}^2(\mathbf{Q}) + 6 f_{\text{H}}^2(\mathbf{Q}) + 2 f_{\text{O}}^2(\mathbf{Q})\right]^{1/2}, \tag{S5}$$

$$f_{\text{CO2}}(\mathbf{Q}) = \left[f_{\text{C}}^2(\mathbf{Q}) + 2 f_{\text{O}}^2(\mathbf{Q})\right]^{1/2}, \tag{S6}$$

where $f_{\text{C}}(\mathbf{Q})$, $f_{\text{H}}(\mathbf{Q})$ and $f_{\text{O}}(\mathbf{Q})$ are the atomic form factors of carbon, hydrogen and oxygen atoms, respectively, which are calculated using a sum of Gaussian functions:

$$f(\mathbf{Q}) = f(Q) = \sum_{i=1}^{4} a_i \mathrm{e}^{-b_i\left(\frac{Q}{4\pi}\right)^2} + c, \tag{S7}$$

where the values of a_i b_i and c are obtained from the International Tables for Crystallography [10]. Figure S4 shows the values of the atomic and molecular form factors for the Q-range in our experiments.

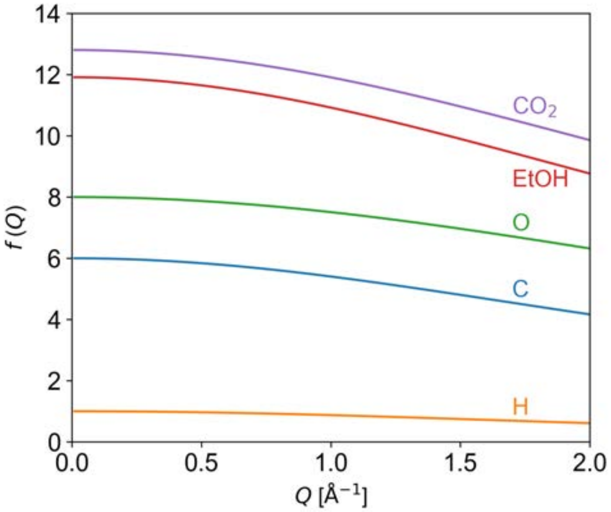

Figure S4: Atomic and molecular form factors for carbon (blue), hydrogen (orange), oxygen (green), EtOH (red) and CO_2 (purple) [10].

Using the mixture's molecular form factor, computed from Eq. S4, the structure factor for the EtOH-CO_2 mixture can be calculated as

$$S(\mathbf{Q}) = \frac{I(\mathbf{Q})}{N f_{\text{mix}}^2(\mathbf{Q})}. \tag{S8}$$

2.1 Structure factor from SAXS

The corrected X-ray scattering intensity from SAXS measurements, $I_{\text{corr}}(Q)$, is obtained through a number of processes, including background subtractions, solid-angle corrections, beam polarization corrections, and angular averaging.

Considering beam attenuation, the number of molecules in the SAXS measurements, N^{SAXS} is

$$N^{\text{SAXS}} = \rho A d \mathrm{e}^{-d/L_{\text{att}}}, \tag{S9}$$

where ρ is the molecular number density of the mixture, A is the area of the illumination region, d is the sample thickness and L_{att} is the attenuation length which depends on the X-ray energy, the fluid's density and its constituent elements [11]. In our experiments, A is constant since the beam size is fixed, and d = $403.3\,\mu\text{m}$ and $430.2\,\mu\text{m}$ for different cones used in the pressure cell, which are measured using X-ray attenuation [1].

The structure factor is calculated as

$$S^{\text{SAXS}}(Q) = \frac{\beta I_{\text{corr}}(Q)}{\rho d \mathrm{e}^{-d/L_{\text{att}}} f_{\text{mix}}^2(Q)}, \tag{S10}$$

where a scaling coefficient β is introduced to normalize the scattering intensity to electron units. This scaling coefficient is determined by matching the high-Q peak values in the structure factors between SAXS and MD results, and is kept constant for the corresponding series of measurements.

2.2 Structure factor from MD simulations

Since the EtOH force field employs a simplified four-site molecule model [12], where the methyl and methylene groups are represented as united atoms, we reconstruct the full-atom EtOH geometry in each simulation snapshot before calculating the structure factor. This is done by aligning and matching the position and orientation of the hydroxyl group between the united-atom and full-atom geometries, ensuring that the reconstructed geometry captures the detailed intramolecular structure necessary for accurate scattering calculations. This approach allows for a more realistic comparison between simulation results and experimental data.

To calculate the scattering intensity from MD simulations, we first construct a grid of discretized scattering vectors, $\mathbf{Q}$, whose components are integer multiples of $2\pi/L$, where L is the length of the cubic simulation box. The Fourier transform of the electron density field, $E(\mathbf{Q})$, is then computed as

$$E(\mathbf{Q}) = \sum_{j=1}^{N_a} f_j(\mathbf{Q}) \mathrm{e}^{\mathrm{i}\mathbf{Q}\cdot\mathbf{r}_j}, \tag{S11}$$

where $f_j(\mathbf{Q})$ is the atomic form factor of the j-th atom, $\mathbf{r}_j$ is the atom position, and N_a is the number of atoms in the system. The scattering intensity, $I(Q)$, is obtained by:

$$I^{\mathrm{MD}}(Q) = \langle E(\boldsymbol{Q})E^*(\boldsymbol{Q})\rangle \tag{S12}$$

where * denotes the complex conjugate, and $\langle\cdot\rangle$ indicates temporal and angular averaging.

Then, the structure factor is computed using Eq. S8

$$S^{\mathrm{MD}}(Q) = \frac{I^{\mathrm{MD}}(Q)}{N f_{\mathrm{mix}}^2(Q)}, \tag{S13}$$

where N is the number of molecules in the simulation and $f_{\mathrm{mix}}^2(Q)$ is the molecular form factor of the mixture defined in Eq. S4.

2.3 Partial structure factor from MD simulations

To separate the total structure factor into partial structure factors, we first compute the partial electron density field of each component as the sum of the atomic electron density fields that belongs to the molecular species

$$E_{\mathrm{EtOH}}(\mathbf{Q}) = \sum_{j\in\mathrm{EtOH}} f_j(\mathbf{Q}) \mathrm{e}^{\mathrm{i}\mathbf{Q}\cdot\mathbf{r}_j}, \tag{S14a}$$

$$E_{\mathrm{CO2}}(\mathbf{Q}) = \sum_{j\in\mathrm{CO2}} f_j(\mathbf{Q}) \mathrm{e}^{\mathrm{i}\mathbf{Q}\cdot\mathbf{r}_j}. \tag{S14b}$$

Then, the partial scattering intensity for a species pair is calculated as [13, 14]

$$I_{\text{EtOH-EtOH}}(Q) = \langle E_{\mathrm{EtOH}}(\mathbf{Q})E_{\mathrm{EtOH}}^*(\mathbf{Q})\rangle\,, \tag{S15a}$$

$$I_{\text{CO2-CO2}}(Q) = \langle E_{\mathrm{CO2}}(\mathbf{Q})E_{\mathrm{CO2}}^*(\mathbf{Q})\rangle\,, \tag{S15b}$$

$$I_{\text{EtOH-CO2}}(Q) = I_{\text{CO2-EtOH}}(Q) = \langle \Re[E_{\mathrm{EtOH}}(\mathbf{Q})E_{\mathrm{CO2}}^*(\mathbf{Q})]\rangle\,, \tag{S15c}$$

where $\Re$ represents the real part of the complex product. The partial structure factor is obtained by normalizing the partial scattering intensity with the species' molecular form factor [15]

$$S_{\text{EtOH-EtOH}}(Q) = \frac{I_{\text{EtOH-EtOH}}(Q)}{Nxf^2_{\text{EtOH}}(Q)}, \tag{S16a}$$

$$S_{\text{CO2-CO2}}(Q) = \frac{I_{\text{CO2-CO2}}(Q)}{N(1-x)f^2_{\text{CO2}}(Q)}, \tag{S16b}$$

$$S_{\text{EtOH-CO2}}(Q) = S_{\text{CO2-EtOH}}(Q) = \frac{I_{\text{EtOH-CO2}}(Q)}{N[x(1-x)]^{1/2}f_{\text{EtOH}}(Q)f_{\text{CO2}}(Q)}. \tag{S16c}$$

3 Force fields in MD simulations

3.1 Pure substances

In our molecular dynamics simulations of EtOH-CO_2 mixtures, we first validate the force fields for pure EtOH [12] and pure CO_2 [16] by comparing the simulated structure factors to experimental X-ray scattering data, as shown in figure 2(a) and 2(d) in the main text. The mean unsigned errors (MUEs) of the simulated structure factors with respect to the experimental data over all Q values and temperatures for pure EtOH and pure CO_2 are 4.6% and 6.0%, respectively. The good agreement confirms that the force fields for EtOH and CO_2 describe the structures of the pure fluids under supercritical conditions. Moreover, we compare the performance of our employed rigid EtOH force field [12] with the a common flexible model, OPLS-AA [17]. As shown in Figures S5 and S6, the rigid model yields density values that are in closer agreement with NIST reference data and reproduces the experimental structure factor from our SAXS measurements with higher fidelity than the flexible OPLS-AA model.

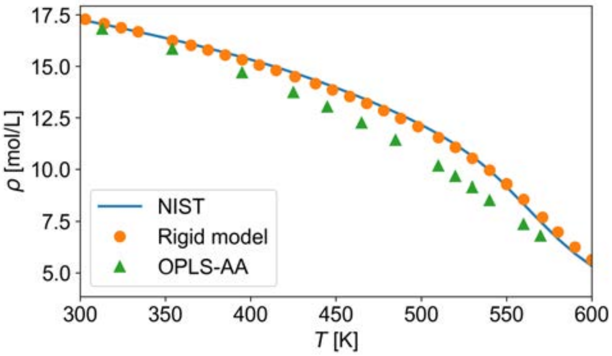

Figure S5: Comparison of the densities of pure EtOH at P = 147 bar with varying temperatures using the rigid force field [12] (dots) and the flexible OPLS-AA force field [17] (triangles). NIST values are plotted as a solid line.

3.2 Optimization for mixtures

For the mixtures, we model the interactions between unlike molecules using the using the modified Lorentz-Berthelot combining rule (Eq. 1 in the main text) with a binary interaction parameter, ξ. Due to limited experimental data of the isothermal liquid-vapor-equilibrium curves at high temperatures, we optimize the value of ξ by fitting the simulated structure factors to our experimental SAXS data. This approach prioritizes

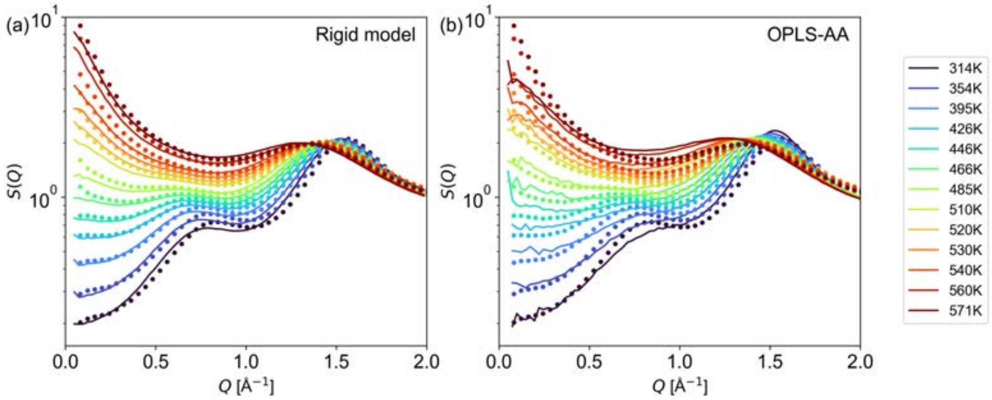

Figure S6: Comparison of structure factors of pure EtOH at P = 147 bar with varying temperatures using the (a) rigid force field [12] and (b) the flexible OPLS-AA force field [17]. SAXS experimental values are plotted as dots, MD simulation values are plotted as lines.

structural accuracy, which is the main focus of our study. Figure S7 and S8 illustrate the detailed comparison between the structure factors from SAXS and MD simulations with varying ξ. The MUEs are plotted in Figure S9.

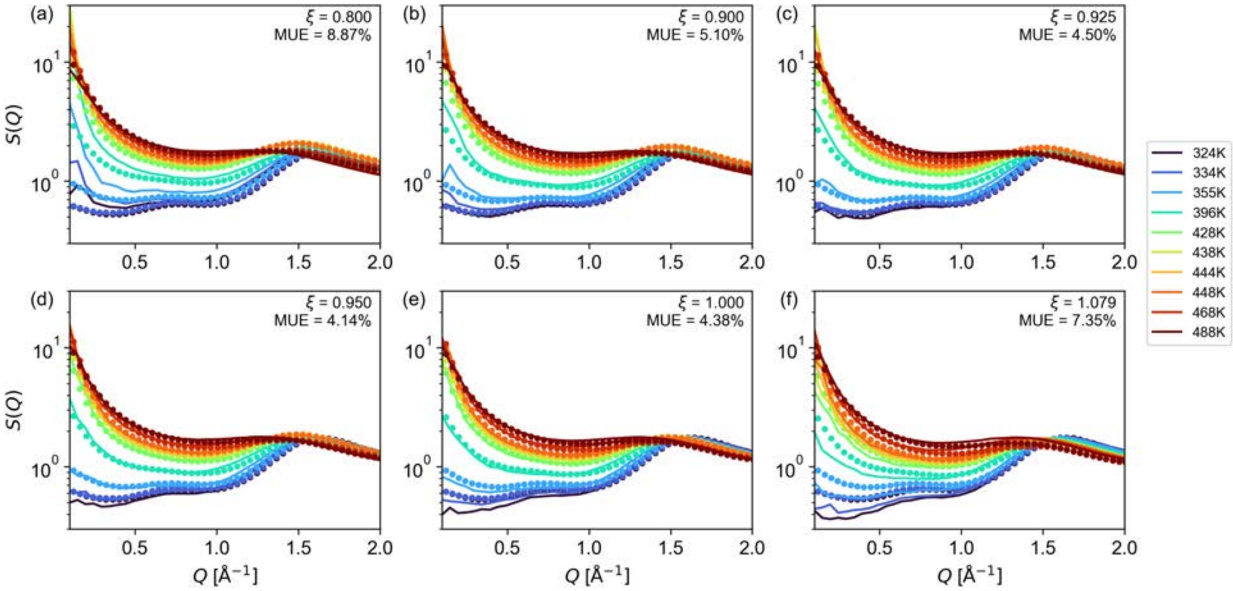

Figure S7: Comparison of structure factors for $x = 0.5$ mixtures between SAXS measurements (dots) and MD simulations (lines) using different binary interaction parameter, ξ, in the modified Lorentz-Berthelot combining rule.

Two key observations can be made from these results. First, the optimal ξ, which corresponds to the lowest mean unsigned error, is not equal to 1. This deviation demonstrates the necessity of modifying the Lorentz-Berthelot combining rule when simulating EtOH-CO$_2$ mixtures. Second, the optimal value of ξ varies depending on the mixture composition. For the EtOH mole fractions $x = 0.5$ and $x = 0.7$, the best-fitting ξ values are 0.95 and 0.90. We note that the force field mixing rule is empirical in nature. As such, the use of a single, composition-independent ξ is not a physical necessity, especially in complex fluids where

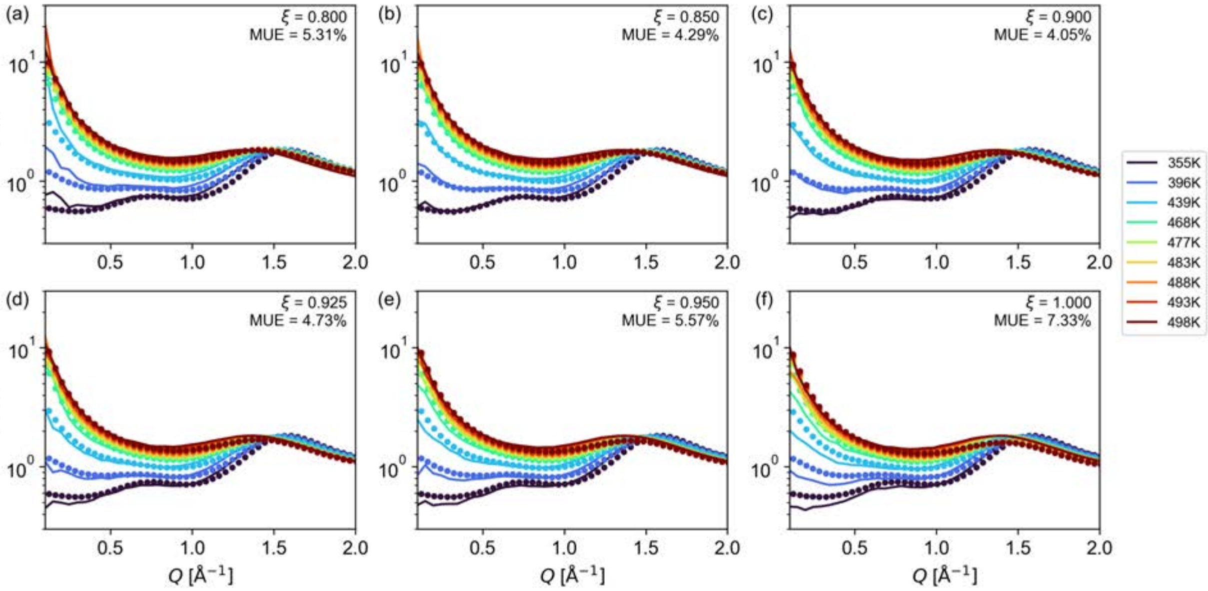

Figure S8: Comparison of structure factors, $S(Q)$, for $x = 0.7$ mixtures between SAXS measurements (dots) and MD simulations (lines) using different binary interaction parameter, ξ, in the modified Lorentz-Berthelot combining rule.

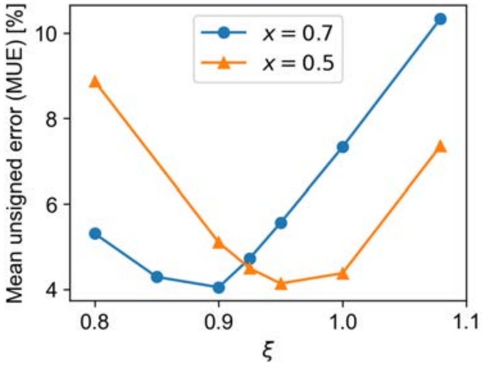

Figure S9: Mean unsigned error (MUE) between simulated structure factors and experimental data for $x = 0.5$ and $x = 0.7$ EtOH-CO$_2$ mixtures, as a function of binary interaction parameter, ξ, in the modified Lorentz-Berthelot combining rule.

mixture interactions exhibit strong composition dependence. Our approach, although pragmatic, offers better fidelity in modeling structure-specific properties of supercritical mixtures under experimentally relevant conditions. Moreover, given our observation that the optimal ξ varies with composition, the development of a broadly transferable potential would require not only a much larger dataset spanning a wide range of compositions, temperatures, and pressures, but also a reevaluation of the combining rule itself. More sophisticated or physically motivated mixing rules may be necessary to capture the complex interactions in supercritical fluid mixtures, which is beyond the scope of our current study.

4 Anomalous properties near the Widom line at the system level

4.1 Radial distribution function

The radial distribution functions (RDF) are calculated using the center-of-mass positions of the molecules in the mixtures. Figure S10 illustrates the RDFs of EtOH-EtOH and CO_2-CO_2 pair interactions for the x = 0.5 and 0.7 mixtures. We observe EtOH self-association as evidenced by the pronounced first peaks in $g_{\text{EtOH-EtOH}}(r)$. In contrast, the first peak of $g_{\text{CO2-CO2}}(r)$ diminishes more rapidly with increasing temperature as shown in Figure S11, indicating that CO_2 structuring is less stable. Notably, the first peak height of $g_{\text{EtOH-EtOH}}(r)$ displays a non-monotonic temperature dependence, exhibiting a local maximum near the Widom line. This trend further supports the persistence of EtOH clustering near the supercritical transition and aligns with the heterogeneities observed in this study.

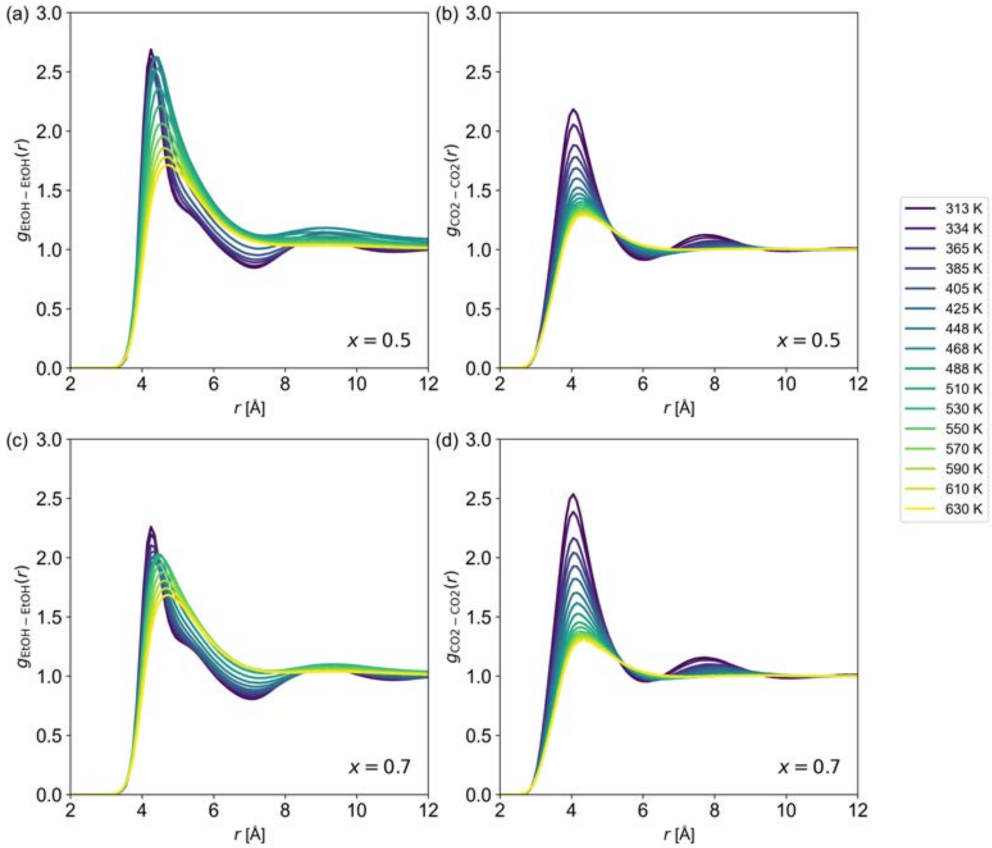

Figure S10: Center-of-mass radial distribution functions of EtOH-EtOH and CO_2-CO_2 pair interactions for (a,b) x = 0.5 and (c,d) x = 0.7 mixtures at varying temperatures along the isobar P = 147 bar.

4.2 Thermodynamic factor

Thermodynamic factor, Γ, is related to the nonideality of a mixture [18]. Here, we compute Γ for the x = 0.5 and 0.7 mixture using Kirkwood-Buff integrals [19, 20]. As shown in Figure S12, Γ exhibits a minimum near the Widom line identified in the work for both two compositions, suggesting strong thermodynamic non-idealities and microscopic heterogeneities near the Widom line.

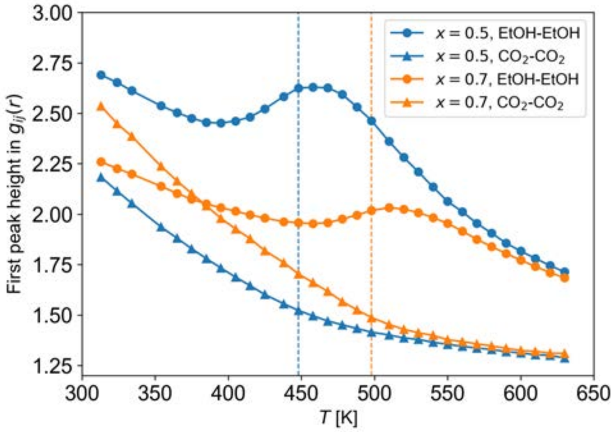

Figure S11: Height of the first peak in $g_{\text{EtOH-EtOH}}(r)$ and $g_{\text{CO2-CO2}}(r)$ (triangles) as a function of temperature for x = 0.5 (blue) and x = 0.7 (orange). The dashed lines indicate the Widom line temperatures identified in this work.

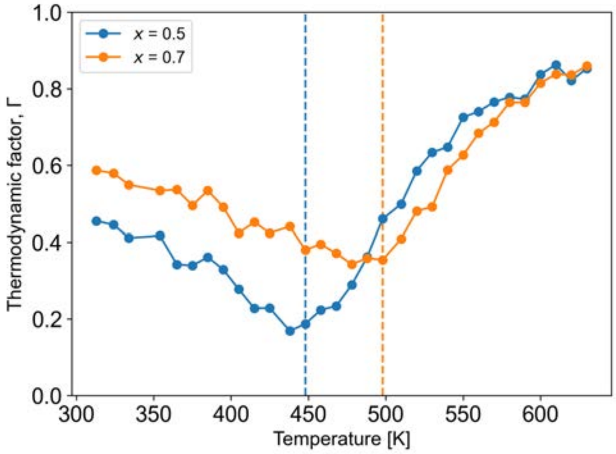

Figure S12: Thermodynamic factor Γ of the supercritical EtOH-CO$_2$ mixtures with EtOH fraction of 0.5 and 0.7 as a function of temperature along the isobar P = 147 bar. The dashed lines indicate the Widom line temperatures identified in this work.

4.3 Thermodynamic response functions and their respective Widom lines

Widom line is originally defined as the locus of maximum correlation length [21, 22]. As the correlation length is not readily available from macroscopic fluid data, the Widom line is often approximated as the locus of maximum thermodynamic response functions, such as density fluctuations ($\rho k_\text{B} T \kappa_T$), constant-pressure heat capacity (c_P), thermal expansion (α_P), and isothermal compressibility (κ_T) [23–28]. The lines of maximum in these response functions are close to each other in the vicinity of the critical point, because all response functions become expressible in terms of the correlation length [21]. These lines deviate from each other when far away from the critical point. In this work, the Widom line is identified as the locus of maximum density fluctuations, since it is directly measured in SAXS experiments.

Here, we compute the density fluctuations, isobaric heat capacity, and thermal expansion coefficient from MD simulations across the studied temperature range, as shown in Figure S13. Notably, for each composition, these thermodynamic response functions exhibit peaks that align with the Widom line temper-

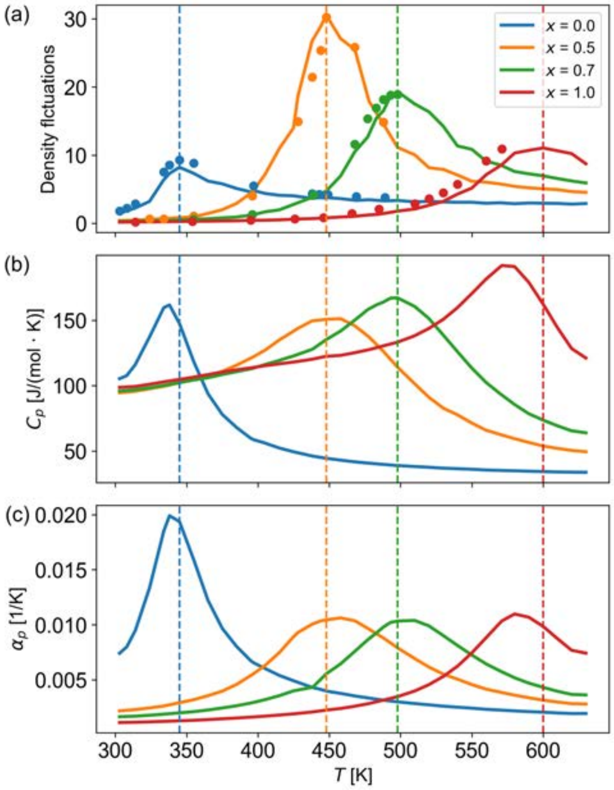

Figure S13: Thermodynamic properties as functions of temperature along the isobar P = 147 bar. (a) Density fluctuations. (b) Isobaric heat capacity. (c) Thermal expansion coefficient. Solid lines are MD simulation results. Dots in (a) are SAXS experimental results derived from $S(0)$. The vertical dashed lines indicate the Widom line temperatures identified as the location of maximum density fluctuations.

atures, which corresponds to enhanced structural heterogeneities and clustering [29]. The relatively large deviation of the peak locations for pure EtOH are attributed to its high reduced pressure $P/P_c = 2.39$, meaning that pure EtOH is far from its critical pressure.

4.4 Self-diffusion coefficient

We compute the self-diffusion coefficients in the mixture from mean-squared displacements. As shown in Figure S14, the self-diffusion coefficients reveal a strong increase across the Widom line, marking the system's transition from a liquid-like to a gas-like regime. Moreover, across the entire temperature range, CO_2 generally diffuses faster than EtOH, reflecting its more uniform spatial distribution compared to the clustered behavior of EtOH. This contrast supports the presence of two dynamically distinct components and highlights how microscopic structure directly impacts macroscopic transport.

5 Cluster identification

The cluster identification algorithm is based on the generalized Hill's energy criterion [30–32]. Two molecules are considered to be physically linked if their interaction energy is stronger than their relative kinetic energy:

$$-e_{ij}^{\mathrm{pot}} \geq \frac{1}{2}\mu \left(\mathbf{v}_i - \mathbf{v}_j\right)^2 , \tag{S17}$$

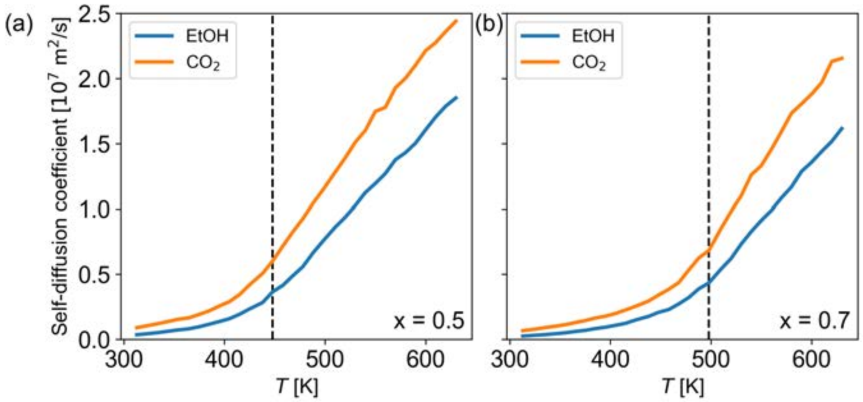

Figure S14: Self-diffusion as a functions of temperature along the isobar $P = 147\,\text{bar}$ for (a) $x = 0.5$ and (b) $x = 0.7$. The vertical dashed lines indicate the Widom line temperatures identified as the location of maximum density fluctuations.

where e_{ij}^{pot} is the interaction potential energy between molecules i and j, $\mu = \frac{m_i m_j}{m_i + m_j}$ is the reduced mass of the two molecules, and $\mathbf{v}_i$ and $\mathbf{v}_j$ are the center-of-mass velocities of molecules i and j, respectively. The interaction potential energy is calculated as:

$$e_{ij}^{\text{pot}} = \sum_{m\in i}\sum_{n\in j}\left[e_{mn}^{\text{LJ}}(r_{mn}) + e_{mn}^{\text{Coul}}(r_{mn})\right], \tag{S18}$$

where m and n are atoms in molecules i and j, respectively, r_{mn} is the distance between them, e_{mn}^{LJ} and e_{mn}^{Coul} are their Lennard-Jones and Coulombic interaction energies, which are defined by the force field.

After identifying all pairs of molecules that satisfy the Hill's energy criterion, the clusters are formed by grouping molecules that are connected using a depth-first search algorithm [33]. The algorithm starts with a seed molecule and iteratively adds neighboring molecules that are connected to the seed molecule. The process continues until no more molecules can be added to the cluster. The algorithm is then repeated with a new seed molecule until all molecules are assigned to clusters. The cluster size, s, is defined as the number of molecules in the cluster. Molecules that are not connected to any other molecules are treated as clusters of size s = 1. The cluster size distribution, $n_c(s)$, is calculated by counting the number of clusters of each size and normalizing it by the total number of clusters in the system.

6 Relative orientation definitions and $g(r, \theta \mid s, \omega)$

To calculate the local entropy with orientational contribution, we define a single orientational angle θ for each molecular pair type [34, 35], as shown in Figure S15: (a) EtOH–EtOH pairs: θ is defined as the angle between the intramolecular O–H vector of the first EtOH molecule and the intermolecular O···O vector connecting the two EtOH molecules. This definition is consistent with the angular criterion used in standard H-bond geometries. (b) EtOH-CO_2 pairs: θ is defined as the angle between the intramolecular O–H vector of the EtOH molecule and the intermolecular O···C vector, capturing the directionality of the electron donor–acceptor interaction. (c) CO_2-CO_2 pairs: θ is defined as the angle between the intramolecular C-O vector of first CO_2 molecule and the intermolecular C···C vector.

To obtain statistically meaningful results, we pool data from all MD snapshots, collecting pairwise distances r, relative angles θ, cluster sizes s, and partial EtOH fractions ω. From these, we construct the ensemble-averaged orientational pair correlation functions $g(r, \theta \mid s, \omega)$. Figure S16 shows representative

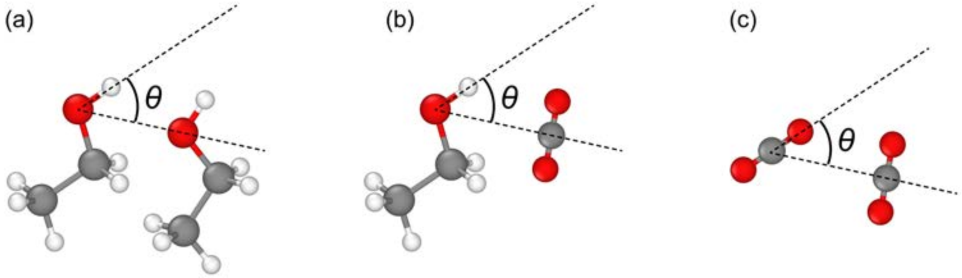

Figure S15: Schematic definitions of the orientational angle θ for different molecular pair types: (a) EtOH–EtOH, (b) EtOH–CO_2, and (c) CO_2–CO_2.

$g(r, \theta \mid s, \omega)$ maps with the same cluster size s = 100 and increasing partial EtOH fractions ω = 0.6, 0.7 and 0.8. The angular preference ($< 30°$) at short distances reflects the H-bonded structure between EtOH molecules. Our results show that the angular preference becomes more focused as ω increases, reflecting stronger orientational ordering.

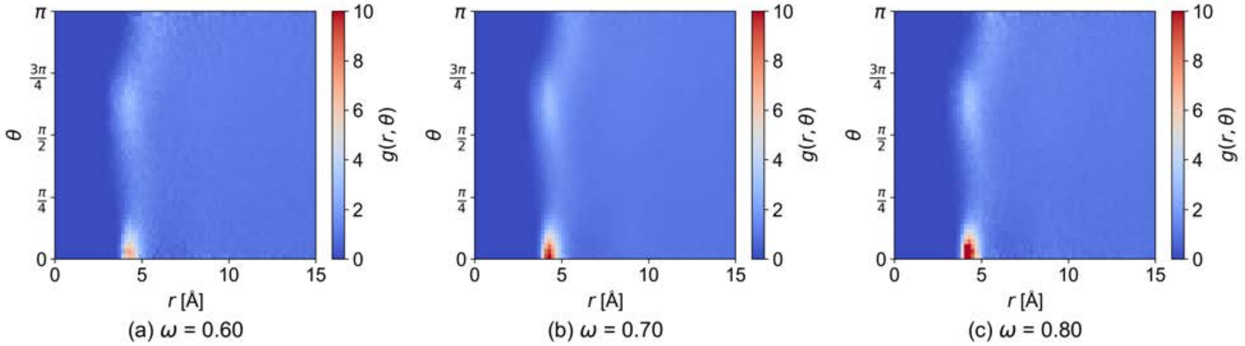

Figure S16: Schematic definitions of the orientational angle θ for different molecular pair types: (a) EtOH–EtOH, (b) EtOH–CO_2, and (c) CO_2–CO_2.

7 Network entropy distribution on cluster size and partial EtOH fraction

When treating the clusters as complex networks, the structural order of a cluster can be characterized by the topology within the network. Based on the Shannon entropy for discrete distributions, the normalized network entropy, $\mathcal{H}$, for a network of size s is defined as [36, 37]:

$$\mathcal{H} = \frac{1}{s \ln(s-1)} \sum_{i=1}^{s} \ln k_i, \tag{S19}$$

where k_i is the degree of node i in the network, i.e., the number of molecules that are connected to the i-th molecule in the cluster through Hill's energy criterion. The normalized network entropy quantifies the heterogeneity of the network's degree distribution, with higher values indicating a more connected network and lower values indicating a more sparse network.

The normalized network entropy $\mathcal{H}(s, \omega)$ is calculated for each cluster in the system, and its variation as a function of cluster size and partial EtOH fraction is shown in Figure S17. The results suggest that at a fixed cluster size, the network entropy increases with partial EtOH fraction, indicating that EtOH-rich clusters

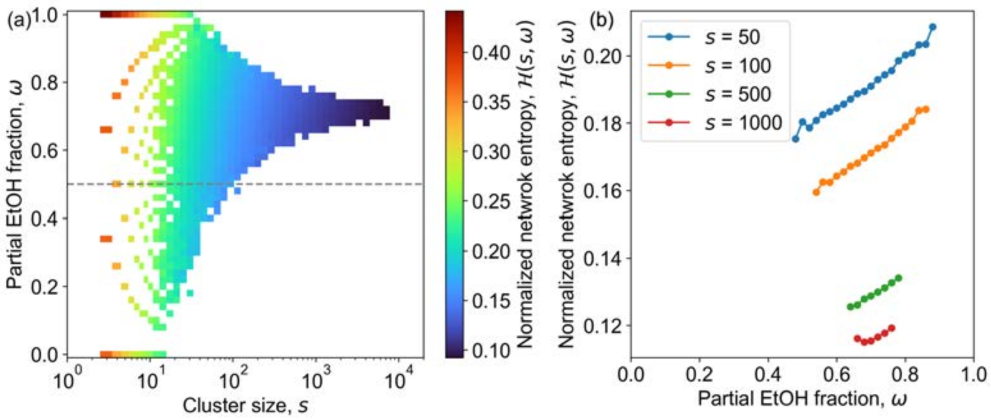

Figure S17: Normalized network entropy $\mathcal{H}(s, \omega)$ as a function of cluster size and partial EtOH fraction in the $x = 0.5$ EtOH-CO_2 mixture at 478 K and 147 bar. (a) The contour plot of $\mathcal{H}(s, \omega)$. (b) The variations of $\mathcal{H}(s, \omega)$ with EtOH fraction at four representative cluster sizes.

tend to form more uniformly connected networks. We note that the trend in network entropy is opposite to that of structural entropy. This arises because network entropy is defined based on the randomness of the network topology: a network with more connections tends to exhibit greater topological randomness, resulting in higher network entropy. Paradoxically, such a highly connected network corresponds to a more ordered cluster structure, which in turn is associated with lower structural entropy. In other words, while increased EtOH content leads to an increase in network entropy, it simultaneously results in a decrease in structural entropy. Therefore, this trend is consistent with the analysis of the local entropy fingerprint in the main text, reinforcing the observation that increased EtOH content leads to a more ordered structure within the clusters.

8 Hydrogen bond distribution on cluster size and partial EtOH fraction

A widely used hydrogen bond criterion in EtOH molecules uses the geometric constraints [38, 39]: (1) the intermolecular O-O distance, $r_{\mathrm{OO}} < 3.5$ Å, (2) the intermolecular O-H distance, $r_{\mathrm{OH}} < 2.6$ Å, and (3) the angle between the O-O alignment and the donor's intramolecular O-H bond, $\varphi < 30°$, as illustrated in figure S18.

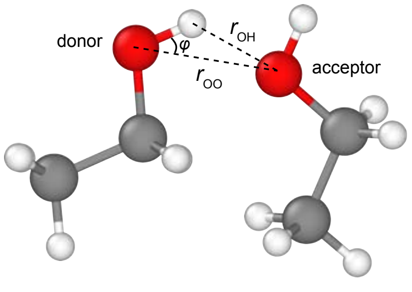

Figure S18: Definitions of geometries in a hydrogen bond between two EtOH molecules.

To validate its applicability in our system, we examine the radial distribution functions (RDF) for O–O and O–H pairs between hydroxyl groups of EtOH molecules. As shown in Figure S19, the applied geometric cutoffs effectively capture the first coordination shell across a range of temperatures. The shaded regions in the RDF plots indicate the spatial thresholds used in the hydrogen bond definition.

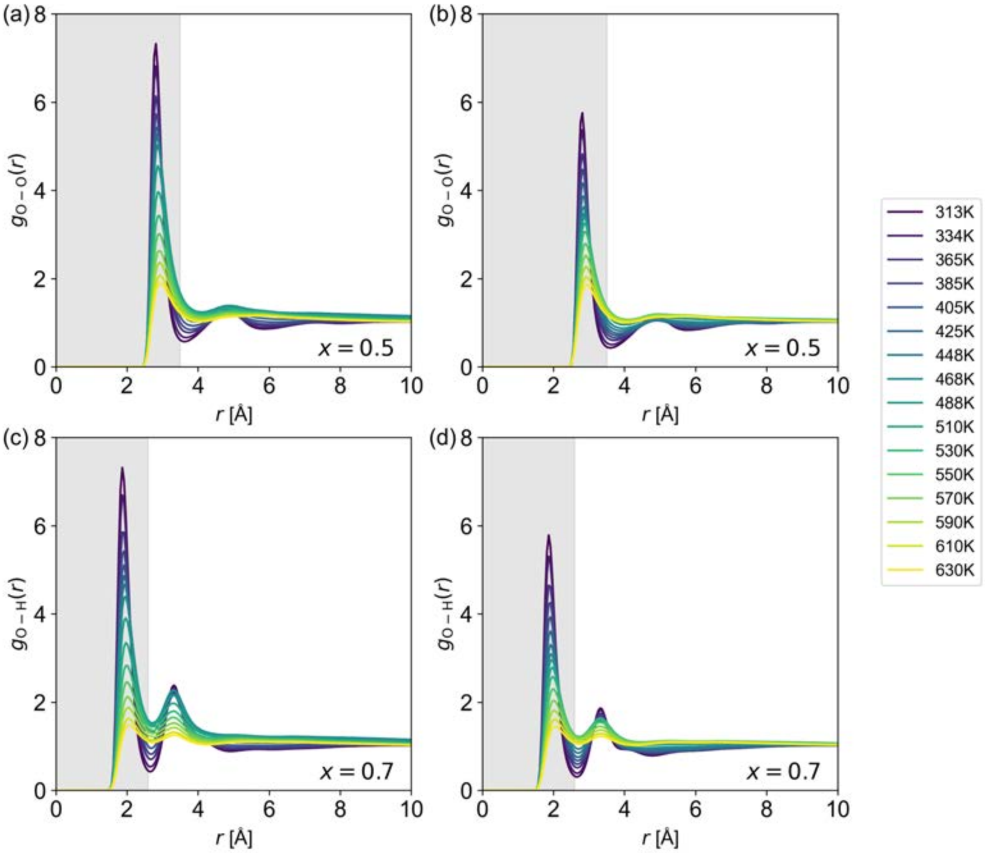

Figure S19: Intermolecular RDFs of O-O and O-H pair within hydroxyl groups for (a,b) x = 0.5 and (c,d) x = 0.7 mixtures at varying temperatures along the isobar P = 147 bar. Shaded regions indicate the distance thresholds used in the H-bond definition , $r_{\mathrm{OO}} < 3.5$ Å,and $r_{\mathrm{OH}} < 2.6$ Å.

Using the geometric criterion, the average number of hydrogen bonds per EtOH molecule, n_{HB}, is calculated for each cluster in the system and its variation as a function of cluster size and partial EtOH fraction is shown in Figure S20. The results indicate that n_{HB} increases with partial EtOH fraction. Hydrogen bonds are inherently directional and impose strict geometric constraints on the relative positions and orientations of molecules. When EtOH molecules form hydrogen bonds, these constraints reduce the configurational freedom of the molecules, thereby promoting a more regular and ordered local structure. This enhanced ordering is consistent with our previous observations that higher EtOH content correlates with increased structural order as measured by both the local entropy and network connectivity analyses.

References

[1] P. Muhunthan, H. Li, G. Vignat, E. R. Toro, K. Younes, Y. Sun, D. Sokaras, T. Weiss, I. Rajkovic, T. Osaka, I. Inoue, S. Song, T. Sato, D. Zhu, J. L. Fulton, and M. Ihme, A versatile pressure-cell design for studying ultrafast molecular-dynamics in supercritical fluids using coherent multi-pulse X-ray scattering, Rev. Sci. Instrum. **95**, 013901 (2024).

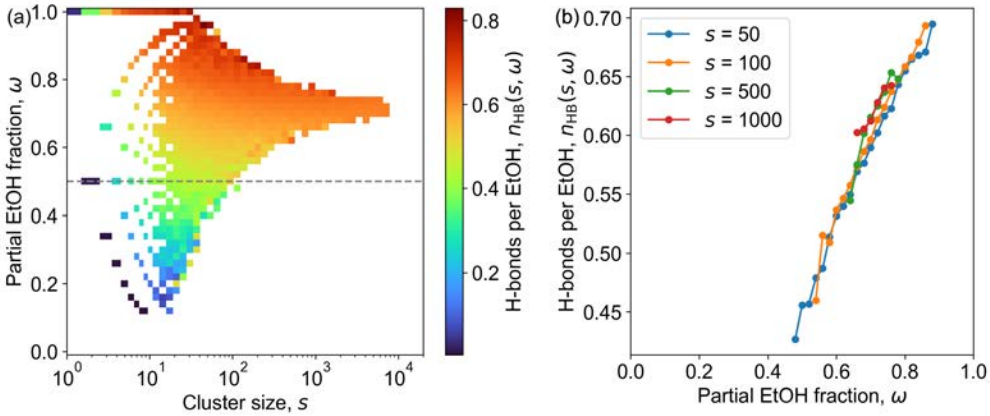

Figure S20: Number of hydrogen bonds per EtOH molecule $n_{\mathrm{HB}}(s,\omega)$ as a function of cluster size and partial EtOH fraction in the $x = 0.5$ EtOH-CO$_2$ mixture at 478 K and 147 bar. (a) The contour plot of $n_{\mathrm{HB}}(s,\omega)$. (b) The variations of $n_{\mathrm{HB}}(s,\omega)$ with partial EtOH fraction at four representative cluster sizes.

[2] J. W. Ziegler, J. G. Dorsey, T. L. Chester, and D. P. Innis, Estimation of liquid-vapor critical loci for CO2-solvent mixtures using a peak-shape method, Anal. Chem. **67**, 456 (1995).

[3] C. Huang, K. T. Wikfeldt, T. Tokushima, D. Nordlund, Y. Harada, U. Bergmann, M. Niebuhr, T. M. Weiss, Y. Horikawa, M. Leetmaa, M. P. Ljungberg, O. Takahashi, A. Lenz, L. Ojamäe, A. P. Lyubartsev, S. Shin, L. G. M. Pettersson, and A. Nilsson, The inhomogeneous structure of water at ambient conditions, Proc. Natl. Acad. Sci. U.S.A. **106**, 15214 (2009).

[4] G. N. I. Clark, G. L. Hura, J. Teixeira, A. K. Soper, and T. Head-Gordon, Small-angle scattering and the structure of ambient liquid water, Proc. Natl. Acad. Sci. U.S.A. **107**, 14003 (2010).

[5] I. H. Bell, J. Wronski, S. Quoilin, and V. Lemort, Pure and Pseudo-pure Fluid Thermophysical Property Evaluation and the Open-Source Thermophysical Property Library CoolProp, Ind. Eng. Chem. Res. **53**, 2498 (2014).

[6] R. Span and W. Wagner, A New Equation of State for Carbon Dioxide Covering the Fluid Region from the Triple-Point Temperature to 1100 K at Pressures up to 800 MPa, J. Phys. Chem. Ref. Data. **25**, 1509 (1996).

[7] J. A. Schroeder, S. G. Penoncello, and J. S. Schroeder, A Fundamental Equation of State for Ethanol, Journal of Physical and Chemical Reference Data **43**, 043102 (2014).

[8] M. L. Huber, E. W. Lemmon, I. H. Bell, and M. O. McLinden, The NIST REFPROP Database for Highly Accurate Properties of Industrially Important Fluids, Ind. Eng. Chem. Res. **61**, 15449 (2022).

[9] A. H. Compton, The distribution of the electrons in atoms, Nature **95**, 343 (1915).

[10] P. J. Brown, A. G. Fox, E. N. Maslen, M. A. O'Keefe, and B. T. M. Willis, Intensity of diffracted intensities, in *International Tables for Crystallography*, Vol. C (2006) pp. 554–595.

[11] J. H. Hubbell and S. M. Seltzer, X-Ray Mass Attenuation Coefficients: NIST Standard Reference Database Number 126 (2004).

[12] T. Schnabel, J. Vrabec, and H. Hasse, Henry's law constants of methane, nitrogen, oxygen and carbon dioxide in ethanol from 273 to 498 K: Prediction from molecular simulation, Fluid Ph. Equilib. **233**, 134 (2005).

[13] S. Mohanty, C. B. Cooper, H. Wang, M. Liang, and W. Cai, Computational approaches to model X-ray photon correlation spectroscopy from molecular dynamics, Modelling Simul. Mater. Sci. Eng. **30**, 075004 (2022).

[14] M. Tomšič, A. Jamnik, G. Fritz-Popovski, O. Glatter, and L. Vlček, Structural properties of pure simple alcohols from ethanol, propanol, butanol, pentanol, to hexanol: Comparing Monte Carlo simulations with experimental SAXS data, J. Phys. Chem. B **111**, 1738 (2007).

[15] N. W. Ashcroft and D. C. Langreth, Structure of binary liquid mixtures. I, Phys. Rev. **156**, 685 (1967).

[16] J. J. Potoff and J. I. Siepmann, Vapor–liquid equilibria of mixtures containing alkanes, carbon dioxide, and nitrogen, AIChE J. **47**, 1676 (2001).

[17] W. L. Jorgensen, D. S. Maxwell, and J. Tirado-Rives, Development and Testing of the OPLS All-Atom Force Field on Conformational Energetics and Properties of Organic Liquids, J. Am. Chem. Soc. **118**, 11225 (1996).

[18] S. H. Jamali, L. Wolff, T. M. Becker, A. Bardow, T. J. H. Vlugt, and O. A. Moultos, Finite-Size Effects of Binary Mutual Diffusion Coefficients from Molecular Dynamics, J. Chem. Theory Comput. **14**, 2667 (2018).

[19] P. Ganguly and N. F. A. van der Vegt, Convergence of Sampling Kirkwood–Buff Integrals of Aqueous Solutions with Molecular Dynamics Simulations, J. Chem. Theory Comput. **9**, 1347 (2013).

[20] R. Fingerhut and J. Vrabec, Kirkwood-Buff integration: A promising route to entropic properties?, Fluid Ph. Equilib. **485**, 270 (2019).

[21] L. Xu, P. Kumar, S. V. Buldyrev, S. H. Chen, P. H. Poole, F. Sciortino, and H. E. Stanley, Relation between the Widom line and the dynamic crossover in systems with a liquid–liquid phase transition, Proc. Natl. Acad. Sci. U.S.A. **102**, 16558 (2005).

[22] H. E. Stanley, P. Kumar, G. Franzese, L. Xu, Z. Yan, M. G. Mazza, S. V. Buldyrev, S.-H. Chen, and F. Mallamace, Liquid polyamorphism: Possible relation to the anomalous behaviour of water, Eur. Phys. J. Spec. Top. **161**, 1 (2008).

[23] N. Yoshida, M. Matsugami, Y. Harano, K. Nishikawa, and F. Hirata, Structure and properties of supercritical water: Experimental and theoretical characterizations, J **4**, 698 (2021).

[24] P. Gallo, D. Corradini, and M. Rovere, Widom line and dynamical crossovers as routes to understand supercritical water, Nat. Commun. **5**, 5806 (2014).

[25] Y. Du, L. Liu, G. Liao, F. Zhang, and J. E., Density fluctuations and transport properties of supercritical carbon dioxide calculated by molecular dynamics simulation near the Widom line, J. Supercrit. Fluids **200**, 106003 (2023).

[26] Z.-Y. Liu, L. Chen, and H. Chen, Characterization of dynamic fluctuations of CO2 fluid parameters at critical regions near the pseudo-critical line, Phys. Fluids **34**, 062003 (2022).

[27] F. Maxim, C. Contescu, P. Boillat, B. Niceno, K. Karalis, A. Testino, and C. Ludwig, Visualization of supercritical water pseudo-boiling at Widom line crossover, Nat. Commun. **10**, 4114 (2019).

[28] P. F. McMillan and H. E. Stanley, Going supercritical, Nat. Phys. **6**, 479 (2010).

[29] J. Fan, N. Ly, and M. Ihme, Heterogeneous cluster energetics and nonlinear thermodynamic response in supercritical fluids, Phys. Rev. Lett. **133**, 248001 (2024).

[30] T. L. Hill, Molecular clusters in imperfect gases, J. Chem. Phys. **23**, 617 (1955).

[31] R. A. X. Persson, On the physical cluster of nucleation theory: Generalized Hill cluster (2011), arXiv:1111.2930 .

[32] F. Simeski and M. Ihme, Supercritical fluids behave as complex networks, Nat. Commun. **14**, 1996 (2023).

[33] R. Tarjan, Depth-first search and linear graph algorithms, SIAM J. Comput. **1**, 146 (1972).

[34] P. M. Piaggi and M. Parrinello, Predicting polymorphism in molecular crystals using orientational entropy, Proc. Natl. Acad. Sci. U.S.A. **115**, 10251 (2018).

[35] Z. Zou, E. R. Beyerle, S.-T. Tsai, and P. Tiwary, Driving and characterizing nucleation of urea and glycine polymorphs in water, Proc. Natl. Acad. Sci. U.S.A. **120**, e2216099120 (2023).

[36] M. Small, Complex networks from time series: Capturing dynamics, in *2013 IEEE International Symposium on Circuits and Systems (ISCAS)* (2013) pp. 2509–2512.

[37] C. G. S. Freitas, A. L. L. Aquino, H. S. Ramos, A. C. Frery, and O. A. Rosso, A detailed characterization of complex networks using Information Theory, Sci. Rep. **9**, 16689 (2019).

[38] Michael. Haughney, Mauro. Ferrario, and I. R. McDonald, Molecular-dynamics simulation of liquid methanol, J. Phys. Chem. **91**, 4934 (1987).

[39] L. Saiz, J. A. Padró, and E. Guàrdia, Structure and dynamics of liquid ethanol, J. Phys. Chem. B **101**, 78 (1997).